Yukon Geological Survey Miscellaneous Report 9

Report on processing of ZTEM magnetic and EM surveys, Selwyn basin area, Yukon, Canada

Ken Witherley
Condor Consulting, Lakewood, Colorado

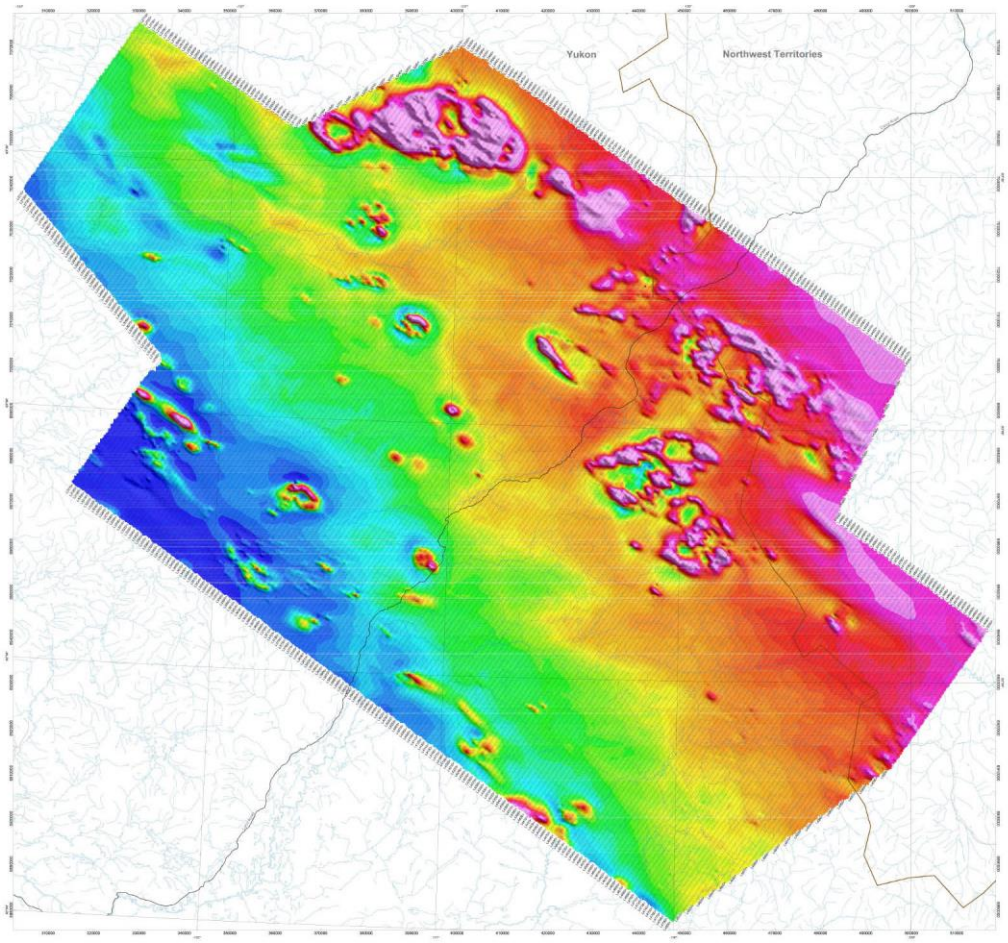

Condor Consulting, Inc.

Yukon Geological Survey

Yukon Energy, Mines and Resources

Published under the authority of the Department of Energy, Mines and Resources, Yukon Government
http://www.emr.gov.yk.ca

Published in Whitehorse, Yukon, 2013

© Department of Energy, Mines and Resources, Government of Yukon

A copy of this report can be obtained by download from: www.geology.gov.yk.ca
or by emailing: geology@gov.yk.ca

In referring to this publication, please use the following citation:
Condor Geophysics, 2013. Selwyn basin geophysics for parts of 105I, 105J, 105K, 105N, 105O, and 105P. Yukon Geological Survey, Miscellaneous Report 9. Report, 65 maps, and data.

Cover photo: Total magnetic intensity (RTP) for parts of 105I, J, K, N, O, and P (1:250 000).

PREFACE

In 2008 Exploration Syndicate Inc. contracted Geotech Inc. to fly a regional-scale ZTEM survey covering a 25,000 km^2 area (1 km line spacing) in the Selwyn basin. The survey footprint straddles the Canol Road in east-central Yukon and overlaps into the western Northwest Territories.

In March 2013 Yukon Geological Survey purchased the survey data, and in May we received approval to distribute the data publicly. As no interpretation was included with the purchase of the data, Condor Consulting Inc. offered to process the data and generate maps, gridded data, and a report. Condor undertook the work at no charge, and their contribution to the project is gratefully acknowledged.

This Miscellaneous Report comprises a number of parts:

- The original survey report produced by Geotech Ltd. describing the data acquisition and processing parameters;
- The raw survey data acquired from Exploration Syndicate Inc.;
- A report summarizing the processing and interpretation undertaken by Condor Consulting;
- A series of maps in *.pdf formats (generated by Condor Consulting); and
- Gridded data (generated by Condor Consulting).

This area is prospective for Sedex-style Pb-Zn-Ag mineralization, and the survey data provide insights into regional structures and plutons in the region. The project was funded by the Canadian Northern Economic Development Agency (CanNor) through their Strategic Investments in Northern Economic Development program.

Carolyn Relf

Director,
Yukon Geological Survey

CONTENTS

1.SUMMARY 1

2.INTRODUCTION 2
ZTEM SURVEY 2

3.PROCESSING AND PRODUCTS 4
PROCESSING 4
ZTEM Data 4
ZTEM 1D and Grid-Based Results 4
2D ZTEM Inversion 5
Magnetic Data Processing 6
3D Magnetic Inversion 6
PRODUCTS 7
Table 3-1 Survey Products 7

4.OUTCOMES 12
DATA QUALITY 12
MAGNETIC RESULTS 12
EM RESULTS 13

5.REFERENCES 15

6.APPENDICES 16
APPENDIX A - INFORMATION ON PROCESSING EM AND MAGNETIC DATA 17
Section 1: Magnetic Processing: ZS and Mag3D 18
Section 2: ZTEM Processing 19
APPENDIX B – ZTEM PRIMER 20
APPENDIX C – DATA AND MAPS 21

1. SUMMARY

This report describes the processing and products generated for a ZTEM airborne EM and magnetic survey carried out for Exploration Syndicate, Inc. by Geotech Ltd. over the Selwyn Basin Yukon-NWT. Condor Consulting, Inc. (Condor) was commissioned by the Yukon Geological Survey (YGS) to process the EM and magnetic data and produce a suite of supplementary map products (in addition to the Geotech provided products) which would facilitate the use of these results. No interpretation was undertaken as part of this program of work.

Respectfully submitted

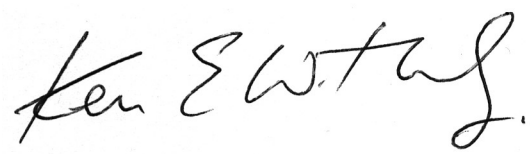

Ken Witherly
October 22, 2013

2. INTRODUCTION

ZTEM SURVEY

Exploration Syndicate, Inc. (ESI) commissioned a ZTEM EM and magnetic survey covering a large part of the Selwyn Basin; primarily in the Yukon but overlapping into the NWT. The survey (designated by ESI as the Selwyn Basin project) was carried out by Geotech Ltd. between May 20 to October 4th, 2008. A total of 24,675 line km of EM and magnetic data were recorded. Full details on the survey can be found in Milicevic et al (2008). The area covered is shown in Figure 1.

Figure 1: Location of ZTEM EM and magnetic survey, Selwyn Basin Project.

The nominal survey line spacing was 1 km which would classify this as a regional class of survey. However, there is a general lack of airborne data of any kind over this area and it is expected that following the release of these results, new insights into the geology, structure and potentially metallogeny of the survey area will accrue.

While the survey area as a whole was flown at a line spacing of 1 lkm, sixteen areas of interest to ESI were flown with 0.5 km in-fill lines. These are shown in Figure 2 and these detailed areas are designated D-1 to D-16.

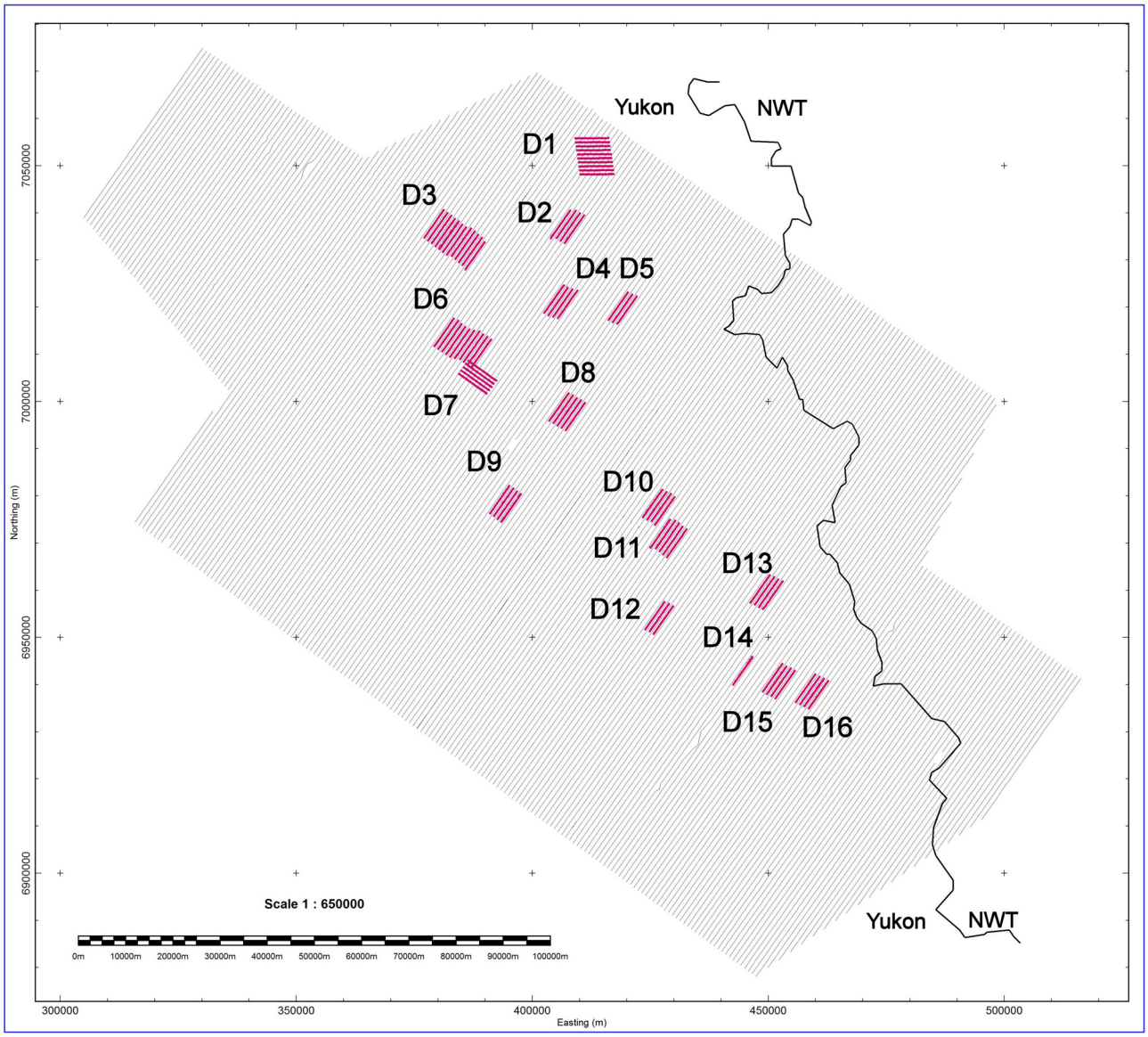

Figure 2: ZTEM survey flight path showing main survey and detailed areas (0. 5 km spaced lines).

.

.

3. PROCESSING AND PRODUCTS

PROCESSING

ZTEM Data

The primary data Geotech provides are the ratios of the Tzx and Tzy (sometimes shortened to X and Y) components for the recovered frequencies; in this case 30, 45, 90, 180 and 360 Hz[1]. The X and Y components are termed the along-line and cross-line components respectively. They in turn provide information about the geology in the cross-line and along-line directions respectively. For each X and Y component, there is both an in-phase (IP) and quadrature (QD) attribute. These form the core data provided in the survey.

The primary form of the ZTEM data is a cross-over response such as shown in Figure 2.

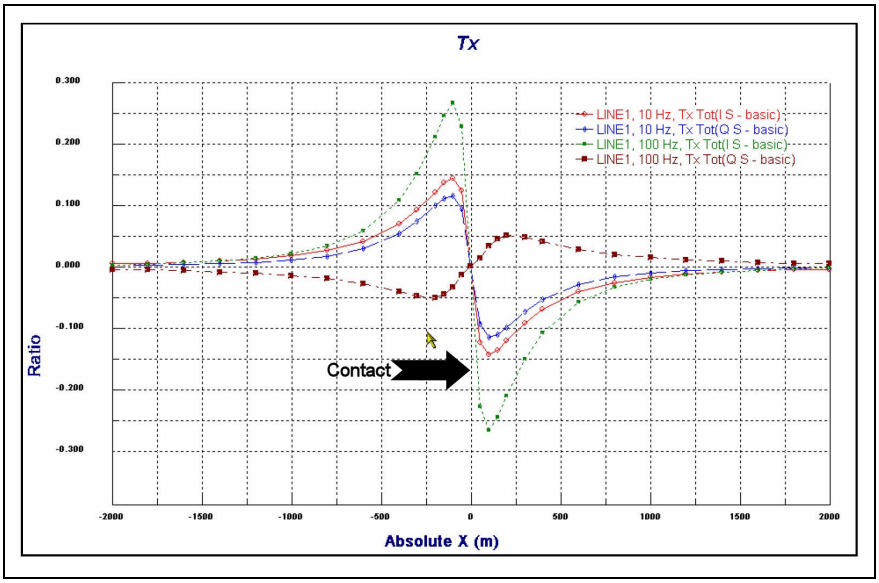

Figure 3: Modeling response of ZTEM over a contact (from Lo 2007).

ZTEM 1D and Grid-Based Results

From the primary ZTEM data, a number of 1D and grid-based products are provided in the report; these various products are listed in Table 3-1 and provided in Appendix C (data & maps). The primary data (1D results) are typically displayed as profiles. Geotech generates a suite of the grid-based products which are derived from the profile data (Milicevic et al 2008). The Geotech report provides definitions of how these are created. The primary purpose of the grid products is to simplify the primary outcomes by merging X and Y components and converting the cross-over style re-

[1] In this survey the 360 Hz signal was the highest signal recovered.

sponse to a positive peak response (over a contact) similar to what the Fraser filter performs for VLF-EM data.

The grids are very useful as they provide what are the highest resolution outcomes of the survey in terms of capturing the spatial changes within the AFMAG fields in the survey area. The processing undertaken is also relatively simple (defined in the Geotech report), so the results are fairly easy to examine. These results do, however, contain effects of topography. The primary effect of topography is to induce conductive features on peaks and resistive features in troughs or valleys. Figure 4 shows this effect.

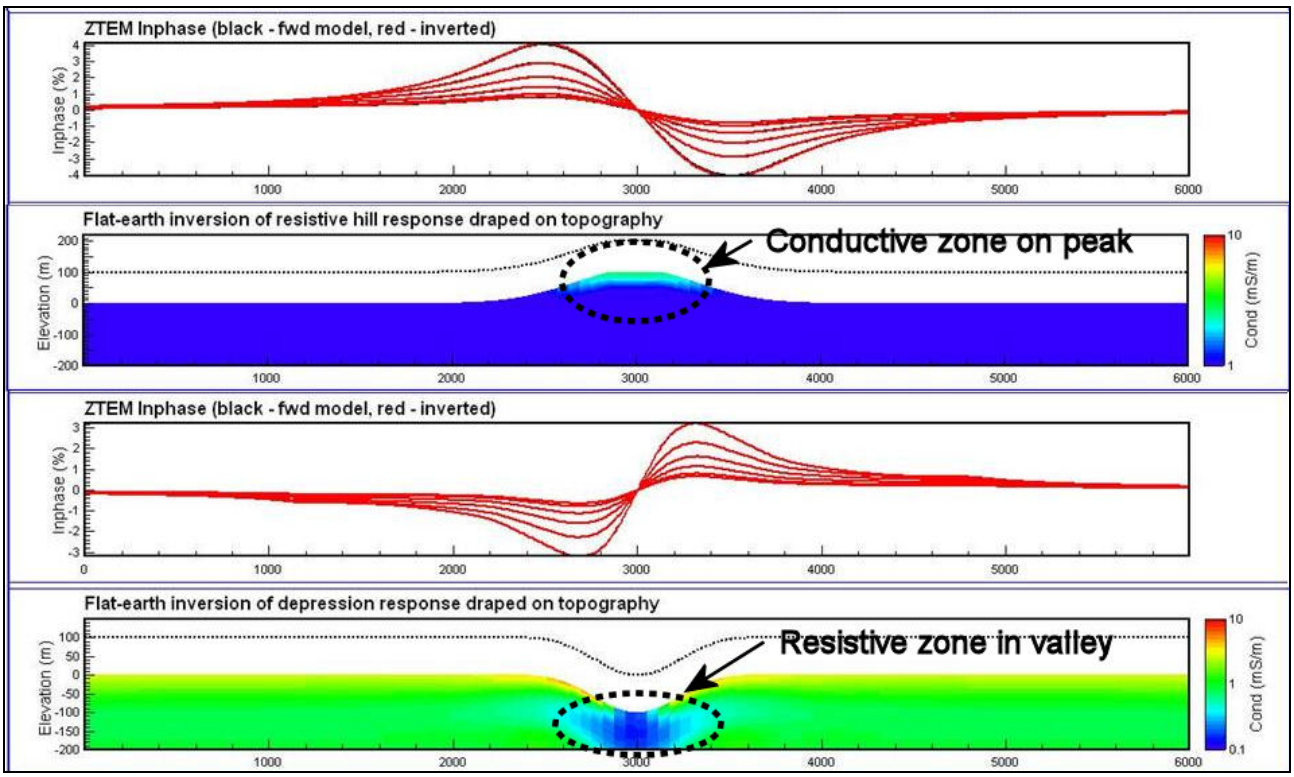

Figure 4: Theoretical modeling of topography and ZTEM responses.

In the present study topography was severe and so the grid products need to be used with caution as they contain what could be a strong topographic ‘over-print’.

2D ZTEM Inversion

The recorded ZTEM data were inverted using a modified 2D MT algorithm to produce a conductivity depth section (CDS). The algorithm models the along-line tipper data Tzx, taking into account that the vertical component is airborne and the horizontal component is measured in a fixed location on the ground. The responses of all frequencies (30-360 Hz) were included in the inversion.

The version of the code used for the present study also removes topographic effects from the data. Further information on the processing of the ZTEM data is provided in Appendix A-Section 2.

Magnetic Data Processing

Additional magnetic grid processing was done using encom pa software[2]; these products are termed the ZS suite. Information pertaining to the ZS processing methodology is provided in Appendix A-Section 1 (Shi and Butt 2004). The ZS products are designated by the form "ZS-'product' where 'product' is the specific outcome. In this report, all magnetic products (including the ZS products) are reduced to pole.

3D Magnetic Inversion

The University of British Columbia (UBC) 3D magnetic inversion program Mag3D, version 4.0, was used for the inversions. The inversions were performed with only the topography surface as model constraints along with the normal UBC style objective function. Information on Mag3D is provided in Appendix A-Section 1.

Condor has produced a background document on the ZTEM technique entitled "ZTEM Primer"; this is provided in Appendix B.

---

[2] Encom V12 PA is a product of PbEncom, a unit of Pitney Bowes Software

PRODUCTS

Table 3-1 lists the products that are provided. All maps are created using the following parameters:

Datum: WGS84

Ellipsoid: WGS84

Projection: UTM Zone 9N

Central Meridian: 129°W

False Northing: 0

False Easting: 500 000

Scale Factor: 0.9996

Table 3-1 Survey Products

FocusMaps: @ 1:250 000

- TMI-RTP
- ZS--Tilt
- ZS-1stVD
- 30 Hz TPR, DT and AppCon
- 180 Hz TPR, DT and AppCon
- DEM[3]
- Geology[4]

---

[3] Canadian Digital Elevation Data (CDED) (2000) Government of Canada, Natural Resources Canada, Earth Sciences Sector, Centre for Topographic Information

[4] Gordey, S.P. 1992 Little Nahanni River (southeast part of Selwyn Basin extending into NWT): 1:250,000 scale GSC Map 1762A Geology from

Gordey, S.P., Pierce, K.L., Fallas, K., Martel, E., and Roots, C.F. (compilers), 2012. GIS compilation for the geology of Sekwi Mountain, Mount Eduni, and northwest Wrigley Lake areas (NTS 105P, 106A, and 95M NW), Mackenzie Mountains, Northwest Territories; Northwest Territories Geoscience Office, NWT Open Report 2012-002. Digital Files; 1:100,000 scale

Gordey, S.P. and Makepeace, A.J. (comp.) 1999: Yukon bedrock geology in Yukon digital geology, S.P. Gordey and A.J. Makepeace (comp.); Geological Survey of Canada Open File D3826 and Exploration and Geological Services Division, Yukon, Indian and Northern Affairs Canada, Open File 1999-1(D); 1:250,000 scale

MultiPlots™ @ 1:170 000 (PDF)

Mini-Plates™: TMI-RTP, ZS-Tilt, 30 Hz Total Phase Rotated (TPR)-In-Phase; 30 Hz AppCon and DEM

On each standard survey line the following content is shown:

- Profiles-EM Z/X 30-360 Hz IP & QD observed with error fit
- Profiles-AppCon: 30 Hz-360 Hz
- Section-2D Conductivity Depth Section-derived from X component + flying height
- Profiles-TMI-RTP, ZS-Tilt, ZS-1stVD
- Section-Susceptibility Depth Section from Mag3D model + flying height
- TrackMap – geology + flight path

Processing report (PDF)

The following files are provided:

-Folder with AppCon grids (Geosoft grid format)

-Mag3D model; UBC format files

-Mag ZS filter suite

-FocusMaps and MultiPlots™ (PDF)

-encompa session file used to produce MultiPlots™

-Processing Report (PDF)

The databases produced for this report are as follows:

8002_final_Dec5_2008 with CDED_DEM edited_ss.gdb

This is a Condor-derived version of the primary Geotech GDB which has been subsampled by a factor of seven. Also the 'broken' lines have been stitched. The EM field structure has been converted to array format.

Produced as part of 2D Occam inversion

Yukon_modconDBS.gdb

-chord length
-cond[1-139]-conductivity of layer mS/m
-D1[1-93]-depth of top of layer
-D2[1-93]-depth of bottom of layer
-DEM (from CDED grid)
-GPSZ_bird
-X
-Y

(Depths in this data base are absolute from sea level)

Yukon_moddat.gdb

-bird height
-chord length
-DEM (from CDED grid)
-moddat[1-10]-modeled IP (1-5) and QD (6-10) for 30,45,90, 180 and 360 Hz;
-obsdat[1-10]-observed IP (1-5) and QD (6-10) for 30,45,90, 180 and 360 Hz;
-X
-Y

Yukon_appcon.gdb

-appcon [1-5]-derived appcon value for 30,45,90,180 and 360 Hz.
-X
-Y
-chord length

Geotech Report 8002

This report was generated by Geotech Ltd. as the final deliverable to the original client of the ZTEM survey; Exploration Syndicate Inc. This report is comprised of four components:

- Report in PDF format

  Survey Report on a Helicopter-Borne Z-Axis Tipper Electromagnetic (ZTEM) and Aeromagnetic Geophysical Survey, Selwyn Basin Yukon, CANADA; for Exploration Syndicate, Inc.; Geotech Ltd Flown in May-October 2008; December 2008

- Folder with Geotech-produced grids
- Folder with Geotech-produced Geosoft maps
- Geosoft GBD 8002_final_Dec5_2008_C.gdb

The Geotech report is generally accurate but the following notes are provided to assist users of this product.

1) The DEM field is normally generated by a combination of radar altimeter on the helicopter and GPS sensors to measure the aircraft (radar) height. In this survey due to the extreme excursions in flying height, the radar altimeter was unable to define the height above ground. This resulted in no DEM field being supplied in the data base. As this field is required for the processing of the EM and magnetic data, Condor used the CDED data base to define a flying height and DEM for the survey.

2) Geotech normally provides a Total Phase Rotated (TPR) result for each frequency but in 2008 this was not yet the standard. Condor has generated a TPR result and added to the final GDB. The TPR is defined as follows by Geotech:

As an alternative, a 90 degree Phase Rotation (PR) technique is also applied to the grids of each individual component (Tzx and Tzy). It transforms bipolar (cross over) anomalies into single pole anomalies with a maximum over conductors, while preserving long wavelength information (Lo et al., 2009). The two orthogonal grids are then usually added to obtain a Total Phase Rotated (TPR) grid for the In-Phase and Quadrature.

Total Phase-Rotation TPR: = PR (*Tzx*) + PR (*Tzy*)

3) Geotech flew most of the lines as 'split lines' due to their length. This original format is preserved in the final data GDB. However, in Condor's provided products, the lines have been merged as generally the off-set was minor.

An example of the Condor-produced MultiPlot is shown in Figure 5.

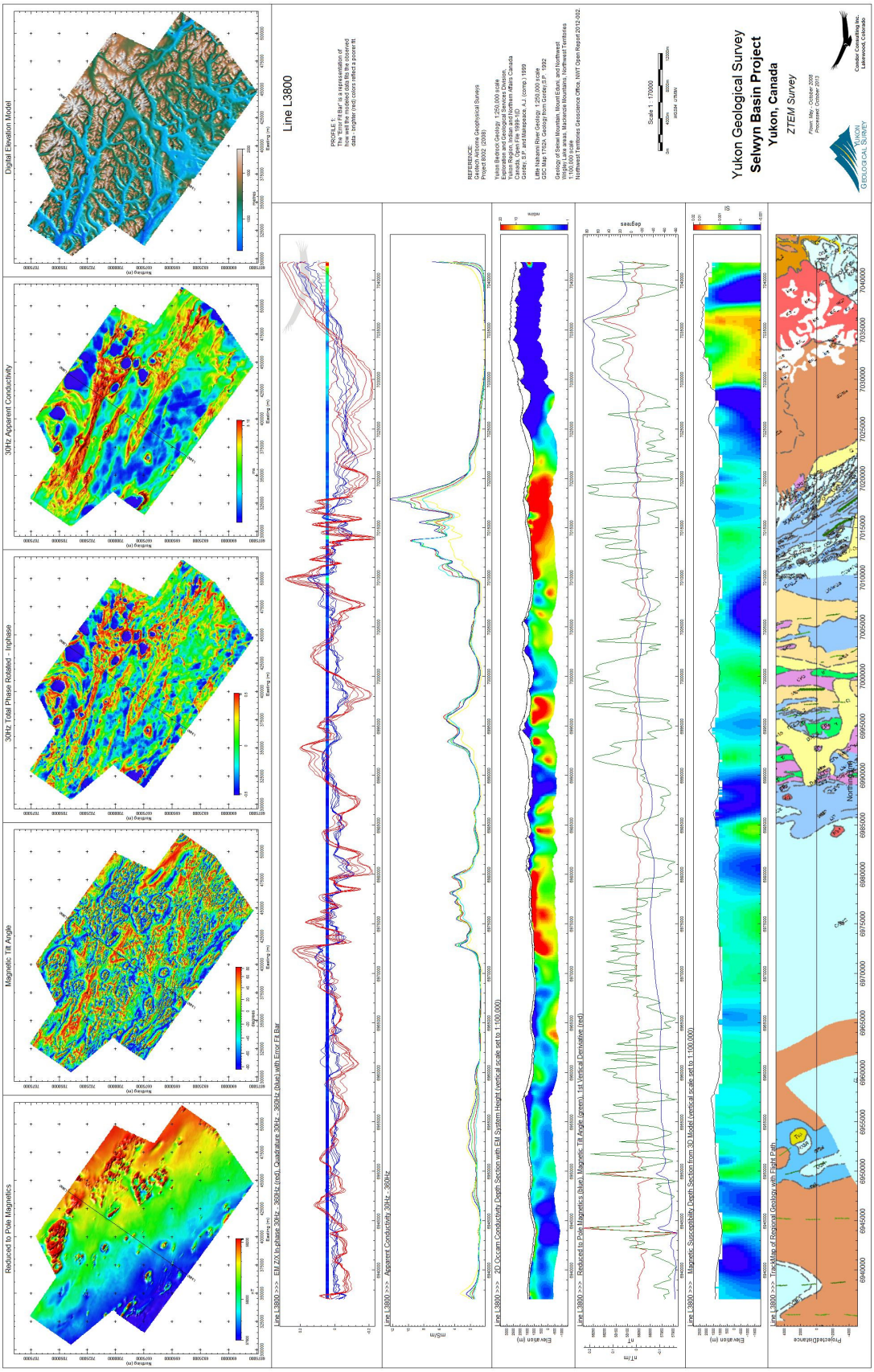

Figure 5: Example of Condor-produced MultiPlot.

4. OUTCOMES

DATA QUALITY

The ZTEM data (EM and magnetics) was deemed to be of reasonable quality. However, Condor noted there were sections of some lines where the EM and magnetic data were not recorded. As noted already, the DEM channel was not provided in the data base but a DEM map was produced. Condor does not know where the data to produce this result came from but we believe our choice of the CDED grid meets the needs of the processing undertaken.

MAGNETIC RESULTS

Figure 6 shows an image of the TMI-RTP. There are a large number of discrete zones of varying sizes and shapes with an overall gradient that trends from high to low moving from the NE to the SW. As well, numerous linear features are apparent in the results (other products provided such as ZS-Tilt accentuates such linears).

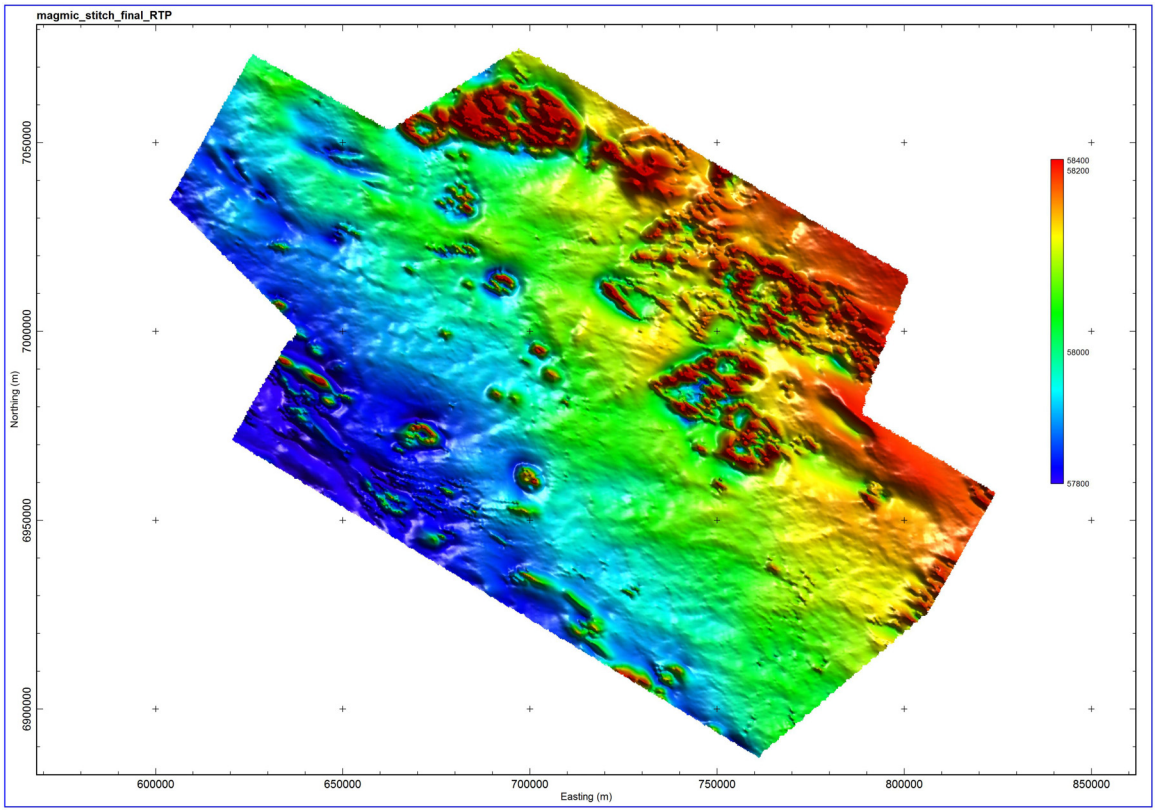

Figure 6: TMI-RTP.

EM RESULTS

Figures 7-9 show EM results; the 45 Hz DT, TPR and AppCon grids. There is a considerable amount of detail in these images which does not appear in the magnetic result. A systematic review of these outcomes will presumably reveal new insights into the structure, lithology and metallogeny of the study area.

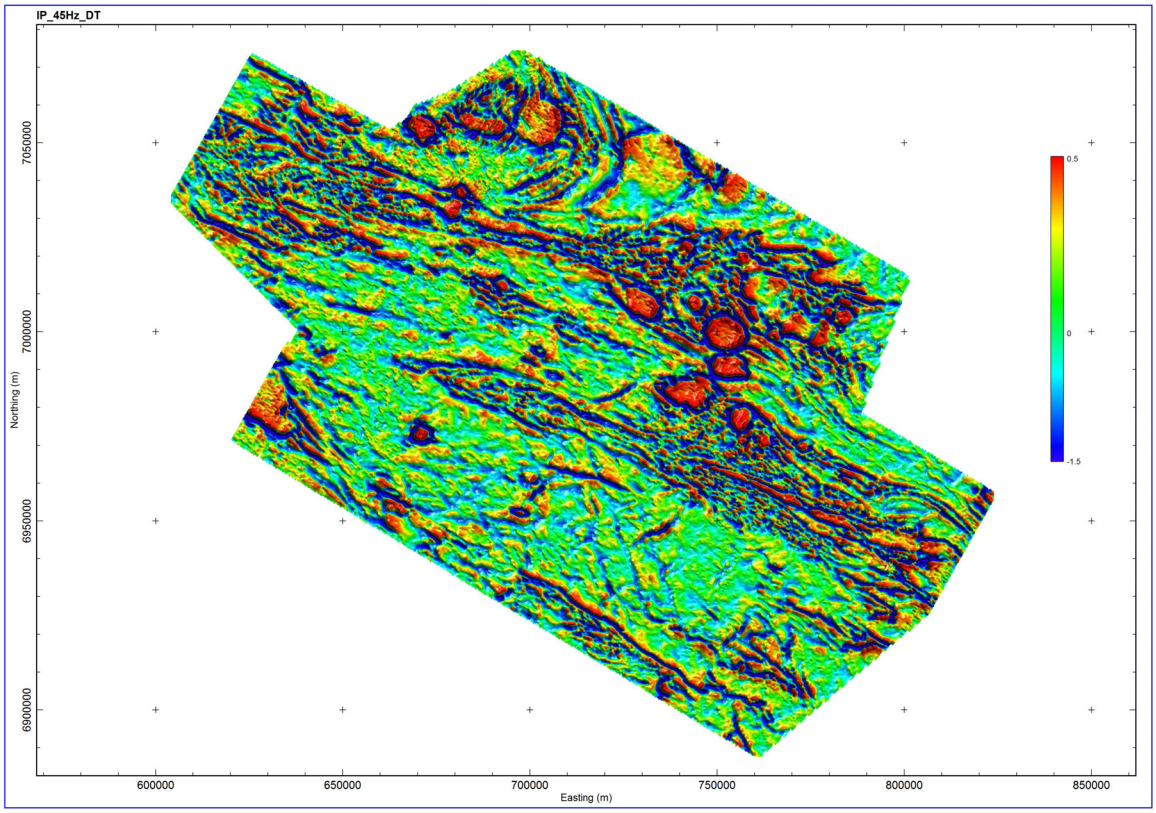

Figure 7: 45 Hz DT grid.

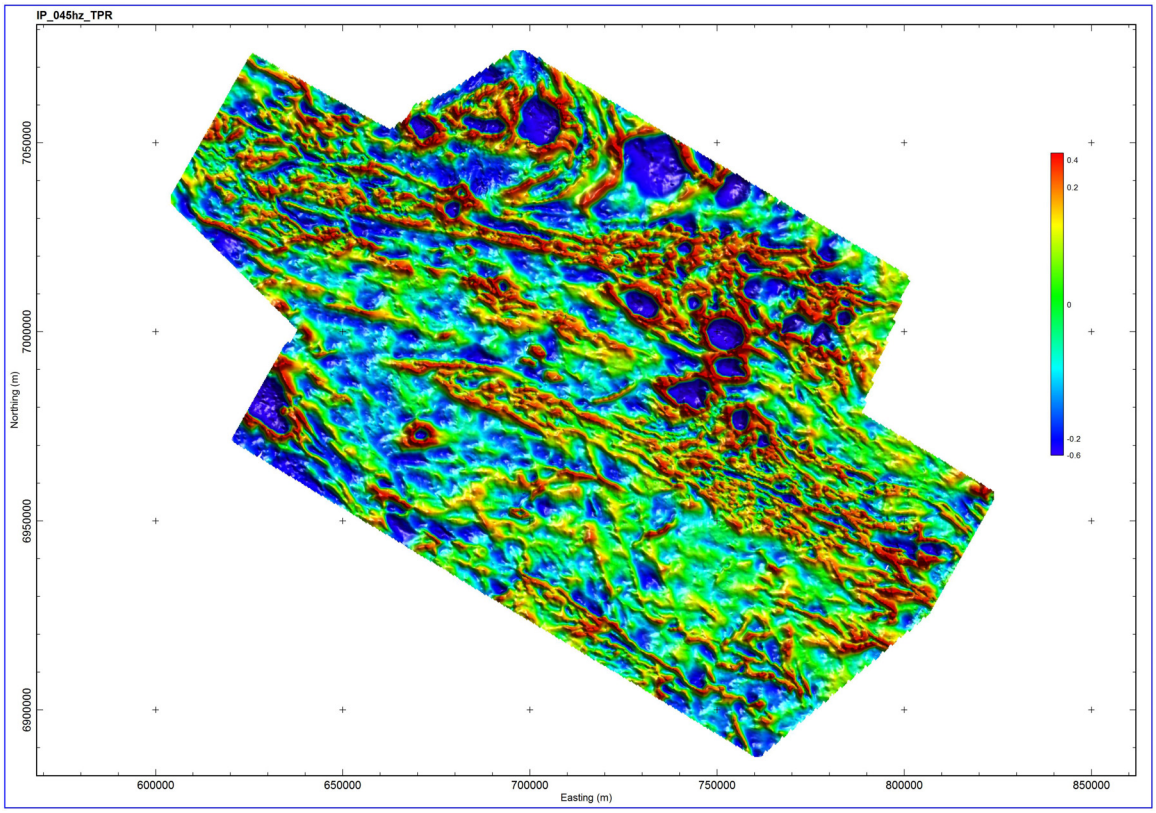

Figure 8: 45 Hz TRP grid.

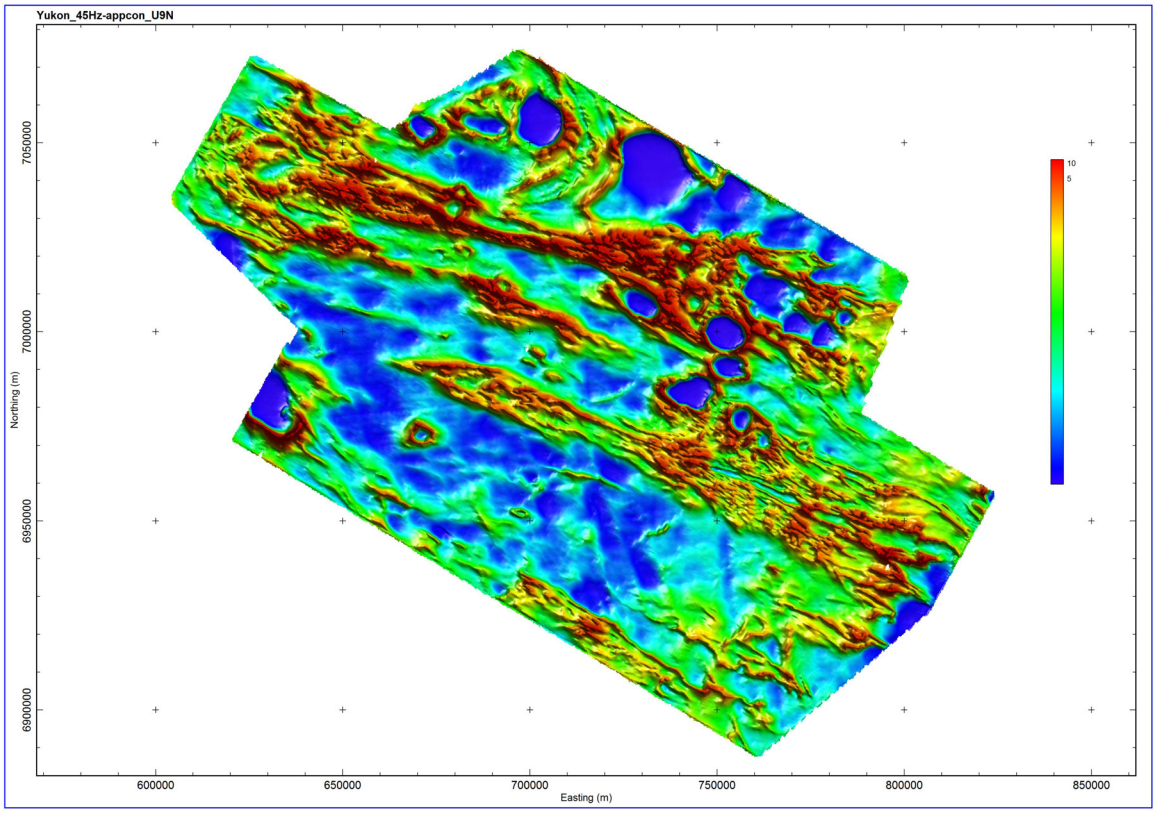

Figure 9: 45 Hz AppCon grid.

5. REFERENCES

Li, Y and Oldenburg D. (1996) 3-D inversion of magnetic data Geophysics, Vol. 61, No. 2 (March-April 1996); P. 394-408, 18 Figs.

Lo, B. (2007), Report on Airborne Geophysical ZTEM and Magnetic Survey for JNR Resources Inc. by Geotech Ltd.; Project # 8244, December 2007.

Sattel, D., Witherly, K., and Becken M., (2010), A brief analysis of ZTEM data from the Forrestania test site, WA: 21st International Geophysical Conference and Exhibition, ASEG, Extended Abstracts.

Shi, Z., and Butt, G., (2004), New enhancement filters for geological mapping; Preview, 111, 87-88.

Milicevic, B., Laloo, S., Legault, J., and Kumar, H (2008), Survey Report on a Helicopter-Borne Z-Axis Tipper Electromagnetic (ZTEM) and Aeromagnetic Geophysical Survey Selwyn Basin Yukon, Canada for Exploration Syndicate, Inc. by Geotech Ltd., Project # 8002, December 2008.

Ward, S., O'Donnell, J., Rivera, R., Ware H., and Fraser D. (1966), AFMAG-Applications and Limitations; Geophysics Vol. 31 No. 3 1966 p 576-605.

6. APPENDICES

APPENDIX A - INFORMATION ON PROCESSING EM AND MAGNETIC DATA

Section 1: Magnetic Processing: ZS and Mag3D

GEOPHYSICS, VOL. 61, NO. 2 (MARCH-APRIL 1996); P. 394-408, 18 FIGS.

3-D inversion of magnetic data

Yaoguo Li* and Douglas W. Oldenburg*

ABSTRACT

We present a method for inverting surface magnetic data to recover 3-D susceptibility models. To allow the maximum flexibility for the model to represent geologically realistic structures, we discretize the 3-D model region into a set of rectangular cells, each having a constant susceptibility. The number of cells is generally far greater than the number of the data available, and thus we solve an underdetermined problem. Solutions are obtained by minimizing a global objective function composed of the model objective function and data misfit. The algorithm can incorporate a priori information into the model objective function by using one or more appropriate weighting functions. The model for inversion can be either susceptibility or its logarithm. If susceptibility is chosen, a positivity constraint is imposed to reduce the nonuniqueness and to maintain physical realizability. Our algorithm assumes that there is no remanent magnetization and that the magnetic data are produced by induced magnetization only. All minimizations are carried out with a subspace approach where only a small number of search vectors is used at each iteration. This obviates the need to solve a large system of equations directly, and hence earth models with many cells can be solved on a deskside workstation. The algorithm is tested on synthetic examples and on a field data set.

INTRODUCTION

Magnetic surveying has been used widely over the years, resulting in a great amount of data with enormous area1 coverage. Magnetic data have been used for mapping geological structures, especially in the reconnaissance stage of exploration, but when used in detailed prospecting, robust and efficient inversion algorithms must be used. However, a principal difficulty with the inversion of the potential data is the inherent nonuniqueness. By Gauss' theorem, if the field distribution is known only on a bounding surface, there are infinitely many equivalent source distributions inside the boundary that can produce the known field. Any magnetic field measured on the surface of the earth can be reproduced by an infinitesimally thin zone of magnetic dipoles beneath the surface. From a mathematical perspective, this means there is no depth resolution inherent in magnetic field data. A second source for nonuniqueness is the fact that magnetic observations are finite in number and are inaccurate. If there exists one model that reproduces the data, there are other models that will reproduce the data to the same degree of accuracy. The severity of the nonuniqueness problem for magnetic data is illustrated in Figures l-3. (The gray scale in all figures indicates susceptibility in SI units for model sections and magnetic data in nT for data plots.) A 3-D dipping prism of uniform susceptibility in Figure 1 produces the surface magnetic field shown in Figure 2, which consists of 441 data. Slices of a 3-D susceptibility model that adequately reproduces the 441 data are shown in Figure 3. That result, however, bears little resemblance to the true model. Susceptibility is concentrated near the surface and displays zones of negative values. This mathematical model solution provides little information about the true structure that is useful.

Faced with this extreme nonuniqueness, previous authors have mainly taken two approaches in the inversion of magnetic data. The first is parametric inversion, where the parameters of a few geometrically simple bodies are sought in a nonlinear inversion and values are found by solving an overdetermined problem. This methodology is suited for anomalies known to be generated by simple causative bodies, but it requires a great deal of a priori knowledge about the source expressed in the form of an initial parameterization, an initial guess for parameter values, and limits on the susceptibility allowed (e.g., Bhattacharyya, 1980; Zeyen and Pous, 1991). Nonuniqueness is not generally an issue because only a small subset of possible models is considered due to the restrictive nature of the inversion algorithm. A related, but unique, approach in Wang and Hansen (1990) assumes polyhedronal causative bodies and

Presented at the 63rd Annual International Meeting, Society of Exploration Geophysicists. Manuscript received by the Editor May 2, 1994; revised manuscript received June 29, 1995.
*UBC-Geophysical Inversion Facility, Dept. of Geophysics and Astronomy, University of British Columbia, 129-2219 Main Mall, Vancouver, BC V6T 1Z4, Canada.
© 1996 Society of Exploration Geophysicists. All rights reserved.

inverts for the position of the vertices of these bodies using the spectrum of the magnetic data. The method is general in principle but has difficulties both in constructing the causative bodies from the recovered vertices and in obtaining the susceptibility distribution.

In the second approach to inverting magnetic data, the earth is divided into a large number of cells of fixed size but of unknown susceptibility. Nonuniqueness of solution is recognized and the algorithm produces a single model by minimizing an objective function of the model subject to fitting the data. Green (1975) minimizes a weighted model norm with respect to a reference model, and this allows the interpreter to guide the inversion by varying the weighting according to the available information. Last and Kubik (1983) choose to minimize the total volume of the causative body so that the final model is compact and structurally simple. Guillen and Menichetti (1984) minimize the moment of inertia of the causative body with respect to the center of gravity or an axis passing through it. Their inversion result is guided by the estimate of the central depth and dip of the causative body. These approaches have merit but they are not flexible enough to handle problems we are concerned with. This is especially true of methods that attempt to collapse the anomalous susceptibility into a single body; such a solution is rarely an adequate representation of geologic structure.

In our inversion approach, we first make a decision about the variable in which the interpretation is to be made, that is, whether susceptibility, log susceptibility, or some function of susceptibility is sought. Next, we form a multicomponent objective function that has the flexibility to generate different types of models. The form of this objective function is such that it can correct for the undesirable aspects of the mathematically acceptable model in Figure 3, namely-the concentration of susceptibility near the surface, the excessive structure, and the existence of negative susceptibilities. Our objective function incorporates an optional reference model so that the constructed model is close to that. It penalizes roughness in three spatial directions, and it has a depth weighting designed to distribute the susceptibility with depth. Additional 3-D weighting functions in the objective function can be used to incorporate further information about the model. Such information might be available from other geophysical surveys, geological data, or the interpreter's qualitative or quantitative understanding of the geologic structure and its relation to the magnetic susceptibility. These 3-D weighting functions can also be used to answer questions about the existence of susceptibility features found from previous inversions. Negative susceptibilities are prevented by making a transformation of

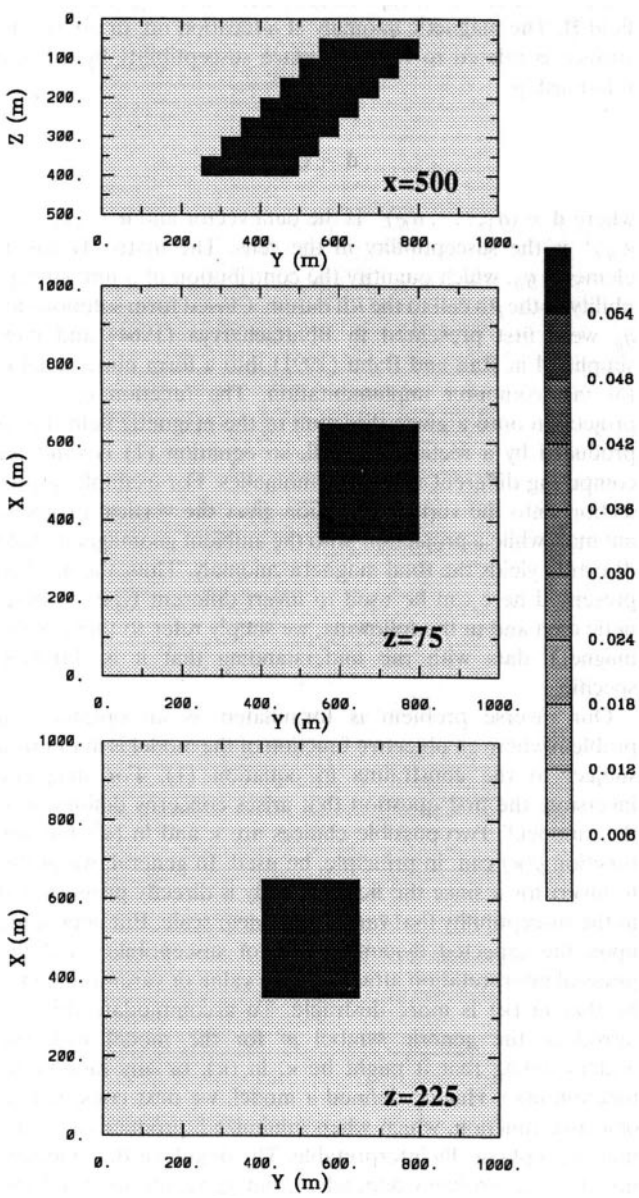

FIG. 1. Slices through a 3-D magnetic susceptibility model composed of a dipping slab in a nonsusceptible half-space. The slab is buried at a depth of 50 m and extends to 400-m depth at a dip angle of 45° . The gray scale indicates the value of magnetic susceptibility in SI units.

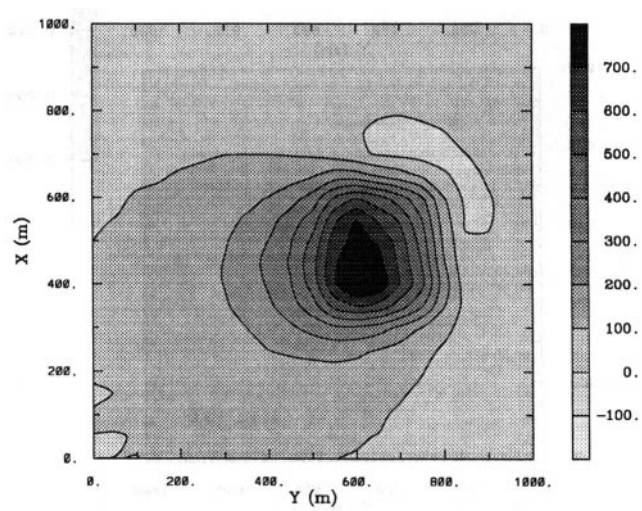

FIG. 2. The total field anomaly produced by the slab model in Figure 1. The inducing field has direction $I = 75°$ and $D = 25°$ and a strength of 50 000 nT. Uncorrelated Gaussian noise, with a standard deviation of 2% of the datum magnitude plus 1 nT, is added to the data. The gray scale indicates the magnetic anomaly in nT.

variables and solving a nonlinear inverse problem. The numerical solution for the inversion is accomplished by dividing the earth into a large number of cells so that relatively complex geologic bodies can be constructed. The computational difficulties often encountered in solving large matrix systems are avoided by working explicitly with a generalized subspace algorithm.

The paper begins by outlining our inversion methodology and empirically estimating parameters for the depth weighting based upon synthetic inversion of single 3-D prisms. Data from two synthetic models are then inverted. The paper concludes by inverting a field data set over a copper-gold porphyry deposit and a subsequent discussion.

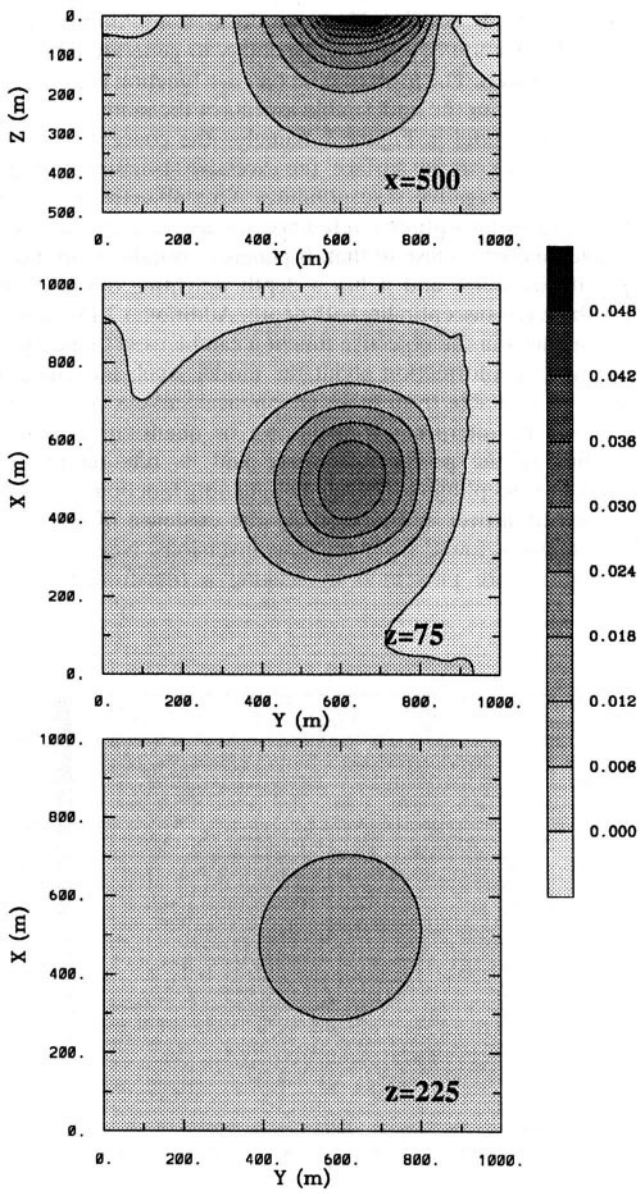

FIG. 3. The susceptibility model constructed by minimizing $\|\boldsymbol{\kappa}\|^2$ subject to fitting the data in Figure 2. As a mathematical solution, this model provides little, if any, information about the subsurface susceptibility distribution. It effectively illustrates the nonuniqueness inherent to the inversion of static magnetic field data.

INVERSION METHODOLOGY

Each magnetic anomaly datum observed above the surface can be evaluated by calculating the projection of the anomalous magnetic field onto a given direction. Let the source region be divided into a set of rectangular cells by an orthogonal 3-D mesh and assume a constant magnetic susceptibility value κ within each cell. Further we assume that there is no remanent magnetization and that the demagnetization effect is negligible. Thus only the induced magnetization is considered. This magnetization is uniform within each cell and is given by the product of the susceptibility and the inducing geomagnetic field $\mathbf{H}$. The magnetic anomaly at a location on, or above, the surface is related to the subsurface susceptibility by a linear relationship

$$\mathbf{d} = \mathbf{G}\boldsymbol{\kappa}, \tag{1}$$

where $\mathbf{d} = (d_1, \ldots, d_N)^T$ is the data vector and $\boldsymbol{\kappa} = (\kappa_1, \ldots, \kappa_M)^T$ is the susceptibility in the cells. The matrix $\mathbf{G}$ has as elements g_{ij}, which quantify the contribution of a unit susceptibility in thejth cell to the ith datum. Closed form solutions for g_{ij} were first presented in Bhattacharyya (1964) and later simplified in Rao and Babu (1991) into a form more suitable for fast computer implementation. The function g_{ij} is the projection onto a given direction of the magnetic field that is produced by a rectangular cell, so equation (1) is valid for computing different magnetic anomalies. For example, a projection onto the vertical direction gives the vertical magnetic anomaly while a projection onto the ambient geomagnetic field direction yields the total magnetic anomaly. Thus, the method presented here can be used to invert different types of magnetic data and in the following, we simply refer to them as the magnetic data with the understanding that it is direction specific.

Our inverse problem is formulated as an optimization problem where an objective function of the model is minimized subject to the constraints in equation (1). For magnetic inversion, the first question that arises concerns definition of the "model." Two possible choices are κ and $\ln(\kappa)$, but any function $g(\kappa)$ can, in principle, be used. In general, we prefer to invert for κ since the field anomaly is directly proportional to the susceptibility that varies on a linear scale. But depending upon the expected dynamic range of susceptibility and the physical interpretation attached to its value or variation, it may be that $\ln(\kappa)$ is more desirable. To accommodate this, we introduce the generic symbol m for the model with the understanding that it might be κ, $\ln(\kappa)$, or any monotonic function $g(\kappa)$. Having defined a model, we next construct an objective function, which when minimized, produces a model that is geophysically interpretable. The details of the objective function are problem dependent, but generally we need the flexibility to be close to a reference model m_0 and also require that the model be relatively smooth in three spatial directions. Here we adopt a right-handed Cartesian coordinate system with x positive north and z positive down. Let the model objective function be

$$\phi_m(m) = \alpha_s \int_V w_s\{w(z)[m(\mathbf{r}) - m_0]\}^2\, dv + \alpha_x \int_V w_x\left\{\frac{\partial w(z)[m(\mathbf{r}) - m_0]}{\partial x}\right\}^2 dv + \alpha_y \int_V w_y\left\{\frac{\partial w(z)[m(\mathbf{r}) - m_0]}{\partial y}\right\}^2 dv + \alpha_z \int_V w_z\left\{\frac{\partial w(z)[m(\mathbf{r}) - m_0]}{\partial z}\right\}^2 dv, \qquad (2)$$

where functions w_s, w_x, w_y , and w_z are spatially dependent weighting functions while α_s, α_x, α_y, and α_z are coefficients that affect the relative importance of different components in the objective function. Here, $w(z)$ is a depth weighting function. It is convenient to write equation (2) as $\phi_m(m) = \phi_{ms} + \phi_{mv}$, where ϕ_{ms} refers to the first term in equation (2) and ϕ_{mv} refers collectively to the remaining three terms that involve variation of the model in three spatial directions.

The objective function in equation (2) has the flexibility of constructing many different models. The reference model m_0 may be a general background model that is estimated from previous investigations, or it could be the zero model. The reference model would generally be included in ϕ_{ms} but can be removed if desired from any of the remaining terms. Often we are more confident in specifying the value of the model at a particular point than in supplying an estimate of the gradient. The relative closeness of the final model to the reference model at any location is controlled by the function w,. For example, if the interpreter has high confidence in the reference model at a particular region, he or she can specify w_s to have increased amplitude there compared to other regions of the model. The weighting functions w_x, w_y , and w_z can be designed to enhance or attenuate structures in various regions in the model domain. If geology suggests a rapid transition zone in the model, then a decreased penalty for variation can be put there, and the constructed model will exhibit higher gradients provided that this feature does not contradict the data. Therefore, the reference model and four 3-D weighting functions allow for the incorporation into the inversion of additional information other than the magnetic data. The additional information can be from previous knowledge about the susceptibility, from other geophysical surveys, or from the interpreter's qualitative or quantitative understanding about the geologic structure and its relation to susceptibility. When this extra information is incorporated, the inversion derives a model that not only fits the data, but more importantly, also has a likelihood of representing the earth. From the viewpoint of magnetic inversion, such an approach allows one to construct a most-likely earth model that uses all available information, and it can also be used to explore the nonuniqueness. These two aspects form the foundation of a responsible interpretation.

The kernels (values of g_{ij}) for the surface magnetic data decay with depth. It is for this reason that an inversion that minimizes $\|m - m_0\|^2 = \int (m - m_0)^2\, \boldsymbol{dv}$ subject to fitting the data will generate a susceptibility that is concentrated near the surface. To counteract the geometric decay of the kernels and to distribute susceptibility with depth, we introduce a weighting of the form $w(z) = (z + z_0)^{-\beta/2}$ into ϕ_{ms}, and optionally include it in ϕ_{mv}. The values of β and z_0 are investigated in the following section, but their choice essentially allows equal chance for cells at different depths to be nonzero.

The next step in setting up the inversion is to define a misfit measure. Here we use the 2-norm measure

$$\phi_d = \|\underset{\sim}{\mathbf{W}}_d(\mathbf{d} - \mathbf{d}^{obs})\|_2^2, \qquad (3)$$

and we assume that the contaminating noise on the data is independent and Gaussian with zero mean. Specifying $\underset{\sim}{\mathbf{W}}_d$ to be a diagonal matrix whose ith element is $1/\sigma_i$ where σ_i is the standard deviation of the ith datum, makes ϕ_d a chi-squared variable distributed with N degrees of freedom. Accordingly $E[\chi^2] = N$ provides a target misfit for the inversion.

The inverse problem is solved by finding a model m that minimizes ϕ_m and misfits the data by a predetermined amount. This is accomplished by minimizing $\phi(m) = \phi_m + \lambda^{-1}(\phi_d - \phi_d^*)$, where ϕ_d^* is our target misfit and λ is a Lagrangian multiplier. To perform a numerical solution, we first discretize the objective function in equation (2) using a finite-difference approximation according to the mesh defining the susceptibility model. This yields

$$\phi_m(\mathbf{m}) = \phi_{ms} + \phi_{mv} = (\mathbf{m} - \mathbf{m}_0)^T \underset{\sim}{\mathbf{W}}_s^T \underset{\sim}{\mathbf{W}}_s(\mathbf{m} - \mathbf{m}_0) + (\mathbf{m} - \mathbf{m}_0)^T(\underset{\sim}{\mathbf{W}}_x^T \underset{\sim}{\mathbf{W}}_x + \underset{\sim}{\mathbf{W}}_y^T \underset{\sim}{\mathbf{W}}_y + \underset{\sim}{\mathbf{W}}_z^T \underset{\sim}{\mathbf{W}}_z)(\mathbf{m} - \mathbf{m}_0)$$
$$\equiv (\mathbf{m} - \mathbf{m}_0)^T \underset{\sim}{\mathbf{W}}_m^T \underset{\sim}{\mathbf{W}}_m(\mathbf{m} - \mathbf{m}_0) = \|\underset{\sim}{\mathbf{W}}_m(\mathbf{m} - \mathbf{m}_0)\|^2, \qquad (4)$$

where $\mathbf{m}$ and $\mathbf{m_0}$ are M- length vectors. The individual matrices $\underset{\sim}{\mathbf{W}}_s$, $\underset{\sim}{\mathbf{W}}_x$, $\underset{\sim}{\mathbf{W}}_y$, $\underset{\sim}{\mathbf{W}}_z$ are calculated straightforwardly once the model mesh and the weighting functions w_s, w_x, w_y, w_z, and $w(z)$ are defined (see Appendix). The cumulative matrix $\underset{\sim}{\mathbf{W}}_m^T \underset{\sim}{\mathbf{W}}_m$ is then formed. For our formulation, the matrix $\underset{\sim}{\mathbf{W}}_m$ is never computed explicitly but we shall use it to derive our final equations.

The inverse problem is solved by minimizing $\phi(\mathbf{m})$ with an appropriate minimization technique. To reduce computation and to invoke positivity, we use a subspace methodology. In its general form, the subspace technique allows the model parameter to be both positive and negative, and thus to ensure positive susceptibility, we may need to invoke a transformation

of variables. Whether or not the transformation is required depends upon the relationship between m_i and κ_i. If $m_i = \ln(\kappa_i)$, so that interpretations are carried out in the logarithmic domain, then no further transformation is necessary since κ_i will be positive irrespective of the sign of m_i. However, if $m_i = \kappa_i$, or $m_i = g(\kappa_i)$, and $g(\kappa)$ is a positive function, then a transformation is required. All possibilities can be handled by introducing a new parameter p, such that $m_i = f(p_i)$, where $f(p)$ is a monotonic function whose inverse and first-order derivative exist. This mapping is then incorporated directly into the subspace minimization process.

Let $\mathbf{p}^{(n)}$ denote the parameter vector at the nth iteration and δp denote the sought perturbation. Performing a Taylor expansion of the perturbed model objective function about the point $\mathbf{p}^{(n)}$ yields

$$\phi_m(\mathbf{p}^{(n)} + \delta p) = \|\underset{\sim}{\mathbf{W}}_m \underset{\sim}{\mathbf{F}} \delta p + \underset{\sim}{\mathbf{W}}_m(\mathbf{m}^{(n)} - \mathbf{m}_0)\|^2, \tag{5}$$

where $\underset{\sim}{\mathbf{F}}$ is a diagonal matrix with elements

$$F_{ii} = \left.\frac{\partial f_i}{\partial p_i}\right|_{p^{(n)}} = \left.\frac{\partial m_i}{\partial p_i}\right|_{p^{(n)}}. \tag{6}$$

A similar Taylor expansion applied to the misfit objective functional $\phi_d(\mathbf{p}^{(n)} + \delta p)$ yields

$$\phi_d = \|\underset{\sim}{\mathbf{W}}_d \underset{\sim}{\mathbf{G}} \underset{\sim}{\mathbf{F}} \delta p + \underset{\sim}{\mathbf{W}}_d(\mathbf{d}(\mathbf{p}^{(n)}) - \mathbf{d}^{obs})\|^2. \tag{7}$$

At each iteration we desire a perturbation that minimizes equation (4) subject to generating a data misfit of $\phi_d = \phi_d^{*(n)}$, where $\phi_d^{*(n)}$ is the target misfit at the nth iteration. In the subspace technique we represent the perturbation as

$$\delta p = \sum_{i=1}^{q} \alpha_i \mathbf{v}_i \equiv \underset{\sim}{\mathbf{V}} \boldsymbol{\alpha}, \tag{8}$$

where the M-length vectors $\mathbf{v}_i$ ($i = 1, q$) are as yet arbitrary. Writing the objective function to be minimized in terms of the coefficients $\boldsymbol{\alpha}$ yields

$$\phi(\boldsymbol{\alpha}) = \|\underset{\sim}{\mathbf{W}}_m \underset{\sim}{\mathbf{F}} \underset{\sim}{\mathbf{V}} \boldsymbol{\alpha} + \underset{\sim}{\mathbf{W}}_m(\mathbf{m}^{(n)} - \mathbf{m}_0)\|^2 + \lambda^{-1}(\|\underset{\sim}{\mathbf{W}}_d \underset{\sim}{\mathbf{G}} \underset{\sim}{\mathbf{F}} \underset{\sim}{\mathbf{V}} \boldsymbol{\alpha} + \underset{\sim}{\mathbf{W}}_d(\mathbf{d}(\mathbf{p}^{(n)}) - \mathbf{d}^{obs})\|^2 - \phi_d^*). \tag{9}$$

Differentiating with respect to the coefficients a yields the final equations

$$\underset{\sim}{\mathbf{B}} \boldsymbol{\alpha} = \mathbf{b},$$

$$\underset{\sim}{\mathbf{B}} = \underset{\sim}{\mathbf{V}}^T \underset{\sim}{\mathbf{F}}^T (\underset{\sim}{\mathbf{G}}^T \underset{\sim}{\mathbf{W}}_d^T \underset{\sim}{\mathbf{W}}_d \underset{\sim}{\mathbf{G}} + \lambda \underset{\sim}{\mathbf{W}}_m^T \underset{\sim}{\mathbf{W}}_m) \underset{\sim}{\mathbf{F}} \underset{\sim}{\mathbf{V}},$$

$$\mathbf{b} = -\underset{\sim}{\mathbf{V}}^T \underset{\sim}{\mathbf{F}}^T \underset{\sim}{\mathbf{G}}^T \underset{\sim}{\mathbf{W}}_d^T \underset{\sim}{\mathbf{W}}_d (\mathbf{d}^{(n)} - \mathbf{d}^{obs}) - \lambda \underset{\sim}{\mathbf{V}}^T \underset{\sim}{\mathbf{F}}^T \underset{\sim}{\mathbf{W}}_m^T \underset{\sim}{\mathbf{W}}_m (\mathbf{m}^{(n)} - \mathbf{m}_0). \tag{10}$$

We note that the matrix $\underset{\sim}{\mathbf{B}}$ is $q \times q$ and therefore the system of equations is easily solved if q is small. At each iteration, we search for a value of λ that yields the target misfit for that iteration. If the target misfit cannot be reached, then the value of λ that achieves the smallest misfit is taken. The search is usually accomplished by solving equation (10) a number of times using different λ values. Once the optimum value of λ is found, the system is solved again to obtain the coefficients $\boldsymbol{\alpha}$ and the model perturbation. This iterative process is continued until the final expected data misfit is achieved and the model objective function undergoes no significant decrease with successive iterations. Subspace vectors $\mathbf{v}_i$ are generated mainly from the gradients of the data and model objective functions. The data are grouped to form subobjective functions of misfit, and a steepest descent vector corresponding to each subobjective function is used as a subspace vector. Partitioning of the data can be formed by grouping data that are spatially close, or by grouping data such that each group has approximately the same contribution to the total data misfit. Both approaches have worked well. The model objective function is partitioned and the gradient vector associated with each of the four components in the model objective function provides additional subspace vectors. In addition, a constant vector is always included, and the selected subspace vectors are orthonormalized before being used in the search. More details on the implementation of the subspace method for the linear inverse problem can be found in Oldenburg and Li (1994).

The final item of practical importance is the specification of the mapping needed to ensure positivity of susceptibility. The positivity is required since we are dealing only with induced magnetization, and the presence of negative susceptibility is negligible in practical geophysical applications. Although our formalism permits the minimization of $m = g(\kappa)$, the two most common situations are $m = \ln(\kappa)$ and $m = \kappa$. When $m = \ln(\kappa)$, we set $p = m$ and hence the matrix $\underset{\sim}{\mathbf{F}}$ in equation (10) is the identity matrix. If $m = \kappa$, we use the two-stage mapping proposed in Oldenburg and Li (1994). It is composed of an exponential segment and a straight line. The two segments are joined together such that the mapping and its first derivative are both continuous. The mapping is given by

$$\kappa = \begin{cases} 0 & p < p_b \\ e^p - \kappa_b & p_b \le p \le p_1, \\ (p - p_1 + 1)e^{p_1} - \kappa_b & p > p_1 \end{cases} \tag{11}$$

where $p = p_1$ is the transition point between exponential and linear segments, and κ_b is selected to be small enough such that susceptibilities smaller than κ_b are not significantly different from zero when the final interpretation is carried out. Here, κ_1 and hence p_1 are chosen so that the ratio $(\kappa_1 + \kappa_b)/\kappa_b$ does not exceed about two orders of magnitude. This prevents the elements F_{ii} from becoming too disparate. We note that the ith row of $\underset{\sim}{\mathbf{V}}$ is multiplied by F_{ii}, and if this value is too small, the ith row of $\underset{\sim}{\mathbf{V}}$ is essentially annihilated and there will be no possibility of adjusting the value of the ith cell. However, if the ratio is too small, the flexibility in the mapping will be restricted and this affects the convergence rate of the algorithm. In the limit that $\kappa_b \to \kappa_1$, the nonlinear mapping degenerates into a linear truncation and the inversion will not converge. However, between the above two extremes, there is a wide range of values for the ratio that can yield a good mapping. Based upon numerical experiments (Oldenburg and Li, 1994), we have chosen a value of 50.0 for this ratio for the examples throughout this paper.

DEPTH WEIGHTING

It is well known that static magnetic data have no inherent depth resolution. For instance, when minimizing $\|m\|_2^2 = \int m^2\, dv$, structures tend to concentrate near the surface regardless of the true depth of the causative bodies. In terms of model construction, this is a direct manifestation of the nature of the kernels whose amplitudes rapidly diminish with depth. The tendency to put structure at the surface can be overcome by introducing a depth weighting to counteract this natural decay. Intuitively, a weighting that approximately compensates for the decay gives cells at different depths equal probability to enter into the solution with a nonzero susceptibility. Before proceeding with the details of the weighting function for magnetic inversion, we illustrate the necessity, and effectiveness, of such a weighting function using a simple 1-D problem.

Consider a set of data $\mathbf{d} = (d_1, \ldots, d_N)^T$ generated from the equation

$$d_i = \int_0^1 g_i(z) m(z)\, dz, \qquad i = 0, \ldots, N, \tag{12}$$

where the kernels are

$$g_i(z) = e^{-az} \cos(2\pi i z).$$

The decay factor e^{-az} causes the constructed model m,(z) to have structure concentrating toward the region of small z in the classic model construction that minimizes $\|m\|^2$, since the model will be a linear combination of the kernels, i.e.,

$$m_c(z) = \sum_{i=0}^{N} \alpha_i e^{-az} \cos(2\pi i z). \tag{13}$$

This is shown in Figure 4a and 4b for two different models. These models are constructed from five data (i = 0,4) to which noise has been added. It is apparent that the constructed model is shifted toward small z where the amplitude of kernels is relatively large. One way to counteract the bias is to seek a solution in model space that is spanned by the nondecaying portion of the kernels, in this case just the cosine functions. The desired model would have the form

$$m_c(z) = \sum_{i=0}^{N} \tilde{\alpha}_i \cos(2\pi i z), \tag{14}$$

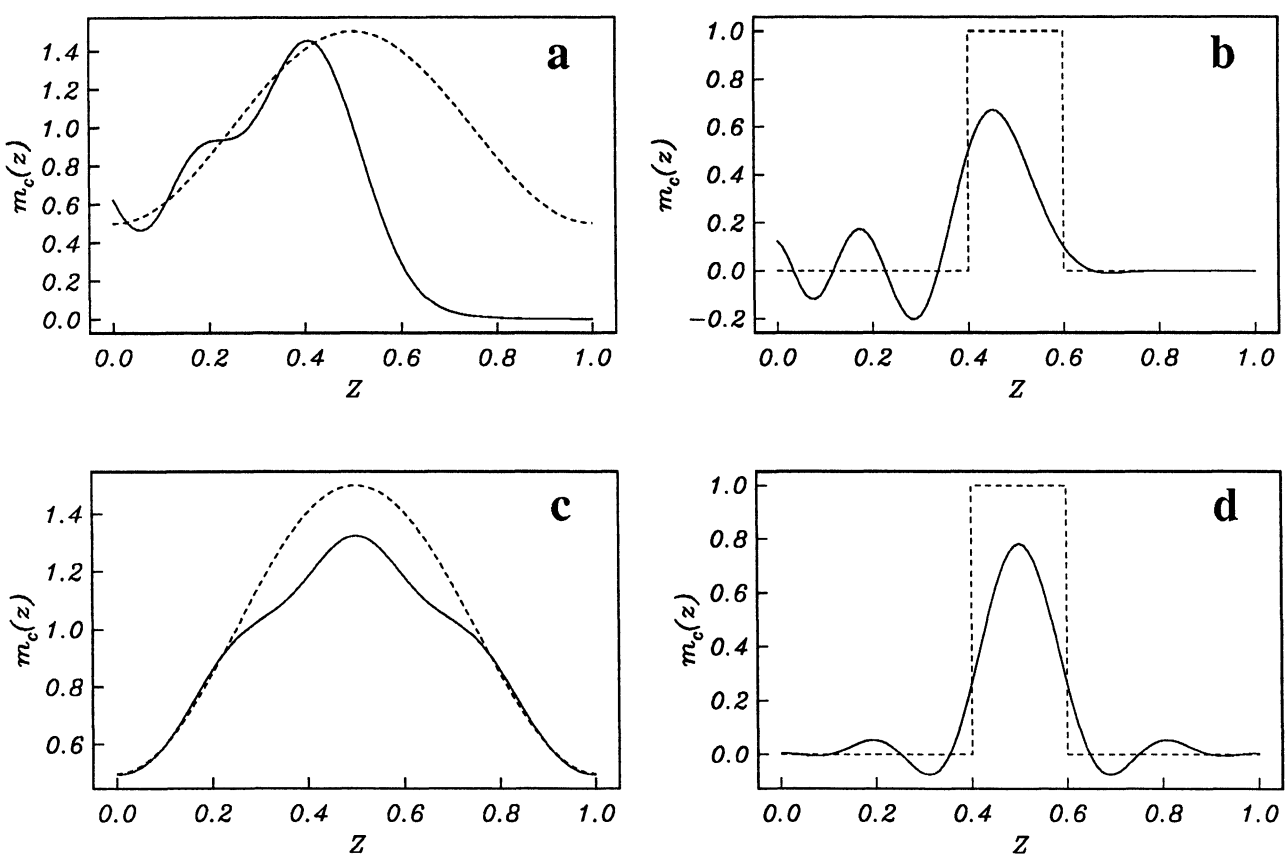

FIG. 4. A 1-D example showing the use of a weighting function in the inversion procedures to counteract the natural decay in the kernel function. In all panels the dashed line shows the true model. Panels (a) and (b) show, for the two different true models, respectively, the model constructed using the original kernel functions with the decaying factor e^{-az}. Notice the shift of the recovered model towards the small z region. Panels (c) and (d) show the weighted models recovered by applying a weighting function $w(z) = e^{-az/2}$. They are better representations of the true model.

where $\tilde{\alpha}_i$ are coefficients. Free from the influence from the decay factor, a model constructed from this set of basic functions should have a better chance of having significantly high values at depth.

We accomplish this by finding an appropriate weighting function $w(z)$. We first rewrite the data equation as

$$d_i = \int_0^1 \frac{g_i(z)}{w(z)} * w(z) m(z)\, dv \equiv \int_0^1 g_i^w(z) m^w(z)\, dv, \quad (15)$$

where $g_i^w(z)$ are the weighted kernels and $m^w(z)$ is the weighted model. Then the inverse problem is solved by minimizing $\|m^w(z)\|^2$ and the solution is given by

$$m_c^w(z) = \sum_{i=0}^{N} \tilde{\alpha}_i g_i^w(z). \quad (16)$$

Dividing $m_c^w(z)$ by the weighting function and substituting in $g_i^w(z)$ yields

$$m_c(z) = \sum_{i=0}^{N} \tilde{\alpha}_i \frac{g_i(z)}{w^2(z)} = \sum_{i=0}^{N} \tilde{\alpha}_i \frac{e^{-az} \cos(2\pi i z)}{w^2(z)}. \quad (17)$$

This equation can be made identical to equation (14) by choosing $w(z) = e^{-az/2}$. Carrying out the weighted inversion for the above two data sets produces models shown in Figures 4c and 4d. They are much better representations of true models.

This methodology is then applied to the inversion of surface magnetic data by finding the appropriate weighting function that counteracts the depth decay of the data kernels. There is no distinct separable factor defining the decay in the kernel, therefore we resort to an empirical estimate. Since the decay rate depends upon the observation height as well as the size and aspect ratios of the cells making up the 3-D model, such estimates are expected to be problem dependent. Numerical experiments indicate that the function of the form $(z + z_0)^{-3}$ closely approximates the kernel's decay directly under the observation point, given a correctly chosen value of z_0. This is consistent with the fact that, to first order, a cubic-shaped cell acts like a dipole source whose magnetic field decays by inverse distance cubed. The value of z_0 can be obtained by matching the function $(z + z_0)^{-3}$ with the kernel function beneath the observation point. Thus, a reasonable candidate for the depth weighting function is given by

$$w(z) = \frac{1}{(z + z_0)^{3/2}}. \quad (18)$$

The susceptibility model constructed by minimizing a model objective function consisting of only ϕ_{ms}, i.e.,

$$\phi_m(m) = \int_V (w(z) m(x, y, z))^2\, dv, \quad (19)$$

subject to fitting the data should place the recovered anomaly at approximately the depth of the causative body. This hypothesis is tested by inverting surface data produced by a susceptible cubic body at three different, depths. The cube is 200 m on a side. Data are calculated over a 21 **X** 21 grid of 50-m spacing in both directions, and 2% Gaussian noise is then added. The observation is assumed to be 1 m above the surface and the inducing field has $I = 75°$, $D = 25°$. The region directly beneath the data grid is taken as the model domain and discretized into 4000 cells (20 cells in each horizontal direction and 10 along depth) of 50 m on a side.

Given the stated data parameters and model discretization, the estimated value of z_0 in the depth weighting function is 25 m. Figure 5 shows the comparison of the kernel beneath a datum point and the function $w^2(z)$. This weighting function is used to invert surface data caused by the susceptible prism, and the results of minimizing ϕ_{ms} are shown in Figure 6. Each panel in the figure is the cross-section through the center of the model obtained by inverting the data set produced by a cube at a different depth. They are rather good recoveries in terms of source depth, which is indicated by the superimposed outline of the true body in each section.

In the above analysis we have established a practical way for estimating an appropriate depth weighting function that distributes the susceptibility more uniformly with depth. The weighting is valid when the model objective function consists only of ϕ_{ms}. In general, we like to include a penalty against roughness and thereby produce a model that is smooth. To incorporate the above weighting scheme in the spatial variations, we make the following argument. Since minimizing ϕ_{ms} tends to provide a reasonable depth distribution, we wish only to improve the model's smoothness while maintaining the depth characteristic. A conceptually consistent approach would be to apply the roughness measures to the weighted model. We form a generic model objective function

$$\phi_m(m) = \alpha_s \int_V w_s \{w(z)[m(\mathbf{r}) - m_0]\}^2\, dv + \alpha_x \int_V w_x \left\{\frac{\partial w(z)[m(\mathbf{r}) - m_0]}{\partial x}\right\}^2 dv + \alpha_y \int_V w_y \left\{\frac{\partial w(z)[m(\mathbf{r}) - m_0]}{\partial y}\right\}^2 dv$$

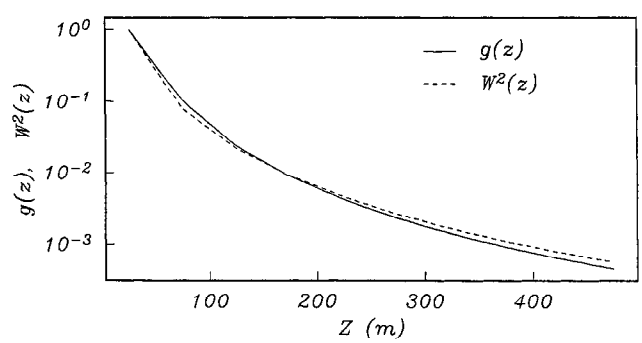

FIG. 5. Comparison of the kernel function (solid) directly beneath the observation point with the estimated curve (dashed) given by $w^2(z) = (z + z_0)^{-3}$ with $z_0 = 25$ m. The source cell is a cube of 50 m on a side. Here, z denotes the depth to the center of the cell. Both curves are normalized for comparison.

$$+ \alpha_z \int_V w_z \left\{ \frac{\partial w(z)[m(\mathbf{r}) - m_0]}{\partial z} \right\}^2 dv, \qquad (20)$$

where the depth weighting is applied inside the derivatives of the roughness components and the reference model m_0 can be removed from any term if desired. This type of depth weighting has proven to work satisfactorily on a number of synthetic examples and is the default choice in our algorithm. The examples to be presented in the following sections all use this depth weighting function.

Before proceeding further, we remark that the above weighting represents only one possibility. One could potentially design a different weighting by incorporating the depth weighting in the usual 3-D weighting functions w_s, w_x, w_y, w_z. Such an approach applies the depth weighting outside the derivative operators directly. However, the decay rate of the depth weighting for each component will be different, and it is difficult to establish a consistent rule for the choice of the different weightings. In addition, the extra set of parameters required by such a weighting scheme introduces more subjectivity into the inversion process. We have not explored this approach in detail; however, it is observed that straightforward inclusion of the depth weighting derived above into the 3-D weighting function in the form of $\int_V w_z w^2(z)\{\partial[m(\mathbf{r}) - m_0]/\partial z\}^2 dv$ can yield reasonable results.

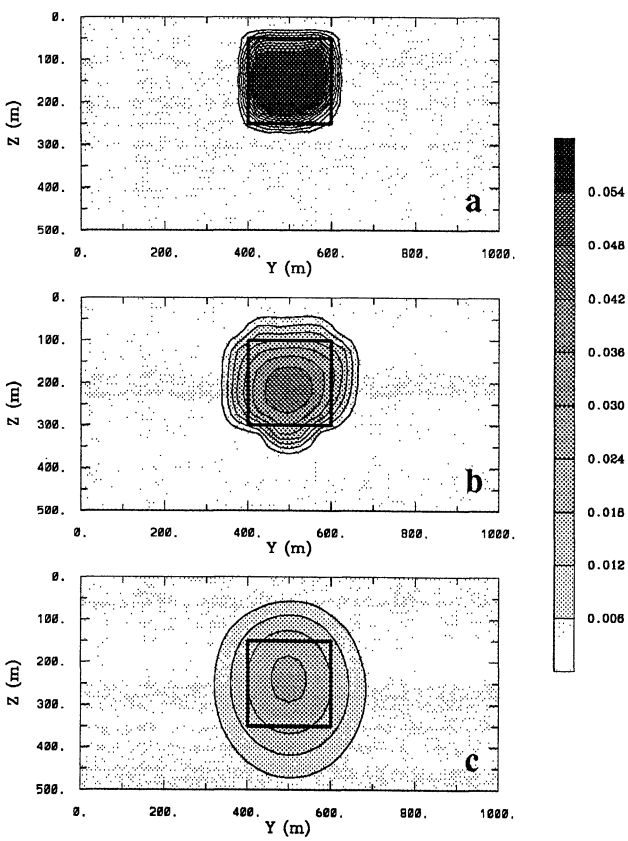

FIG. 6. Cross-sections through the center of the recovered model for a cube at a central depth of 150,200, and 250 m. The cube is 200 m on a side. The inversion uses the weighting function derived from the kernel decay estimated in Figure 5. The true position of the cube is outlined in each cross-section. As the true source depth increases and, as a result, the high-frequency content in the data decreases, the recovered model becomes increasingly smooth and attains a smaller amplitude. However, the depth of the recovered model is close to the true value.

PRACTICAL ASPECTS OF DATA PREPARATION

The data used in the inversion are the residual data obtained by subtracting a regional field from the initial observation. The inversion algorithm has been developed under the assumptions that the surface magnetic anomaly is produced by the induced magnetization only and that there are no remanent magnetization or demagnetization effects present. Incorrect removal of regional field, or any deviation from the above assumptions, is expected to cause a deterioration in the inversion results. Furthermore, the susceptibility distribution is mathematically represented by a piece-wise constant function defined on a user-specified grid of cells. Magnetic sources, however, have a wide range of physical sizes. In some cases, source dimensions will be significantly smaller than the size of cells in the mathematical model. If measurements are taken close to such a source, the resulting anomaly will have a width that is significantly smaller than that produced by a single cell in the mathematical model and this may produce artifacts. We ameliorate this problem by inverting data that have been upward continued to a height approximately equal to the width of the surface cells in the model. We arrive at this conclusion from a numerical experiment. We first generate the magnetic field H_ℓ from a small localized surface source that is assumed to be a cube of width ℓ. At each height h above the surface, a one-parameter inverse problem is carried out to find a uniform susceptibility of a large surface cube that has a width of L and shares a common horizontal center with the small cube. If H_L is the field of the large cell that best reproduces H_ℓ then the misfit functional,

$$r(h) = \frac{\int_{\Delta S} (H_\ell - H_L)^2 \, ds}{\int_{\Delta S} H_\ell^2 \, ds}, \qquad (21)$$

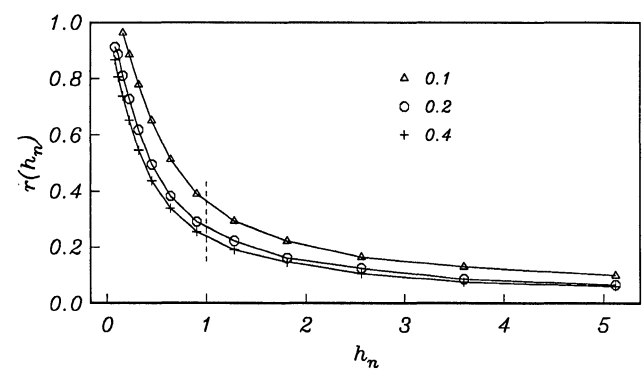

FIG. 7. The misfit between magnetic field as a result of a small cubic source and the field as a result of a larger cubic model cell having a best fitting susceptibility. The numbers indicate the ratio of the cell width. The misfit is plotted as a function of the observation height normalized by the width of the model cell. Note that the misfit decreases rapidly until the height is approximately equal to the width of the model cell, and that it changes slowly thereafter.

can be computed, where ΔS is the surface area of the data map. Figure 7 shows the misfit function $r(h)$ for trial values of ℓ/L = 0.1, 0.2, 0.4. We note that $r(h)$ decreases rapidly until $h \approx L$, and that it changes slowly thereafter. Since the above misfit analysis is a worst case scenario because the contaminating body is located at the surface, the suggestion of upward continuing the data to a height approximately equal to the width of surface cells may be somewhat conservative, and inversionists may want to vary this. However, in many field surveys, magnetically susceptible small bodies exist close to the surface and hence upward continuing the data prior to inversion is prudent.

SYNTHETIC EXAMPLES

As the first example, we invert the total field anomaly data given in the Introduction. The model consists of a 3-D dipping slab buried in a nonsusceptible half-space (slab model). Figure 1 shows three slices through the slab model. The susceptibility of the slab is 0.06 (SI unit). Under an inducing field with a strength of 50 000 nT and a direction at I = 75° and D = 25°, the slab model produces the surface total magnetic anomaly shown in Figure 2, which consists of 441 data over a 21 **X** 21 grid of 50-m spacing. The data have independent Gaussian noise added whose standard deviation is equal to 2% of the accurate datum magnitude plus 1 nT. We invert these 441 noise-contaminated data to recover the susceptibility of an earth model parametrized by 4000 cells of 50 m on a side (20 cells in each horizontal direction and 10 in depth).

The data are partitioned into 49 groups to provide 49 search vectors for the subspace algorithm. In addition, each component in the model objective function provides one basis vector, and a constant vector is included. For the depth weighting, the value of z_0 is estimated as 25 m. The additional 3-D weightings in the objective function are all set to unity. The reference susceptibility model is set to zero. For the nonlinear mapping, we choose κ_b = 0.0002 and κ_1 = 0.01.

First, we invert the data by minimizing an objective function composed only of the ϕ_{ms} and using $m = \kappa$ as the model parameter. A total of 51 subspace vectors are used at each iteration. The inversion reaches the expected misfit in 13 iterations but a few extra iterations are performed in an attempt to further reduce the value of the model objective function while keeping the misfit at the target value. By iteration 18, the objective function is decreasing by less than 1% per iteration, and the process is terminated. The constructed susceptibility model is shown in Figure 8 and can be compared with the true model in Figure 1. The tabular shape of the anomaly and its dipping structure are clear, and the depth extent is reasonably recovered. The amplitude of the recovered model is slightly higher than the true value, but the dip angle inferred from the recovered model is close to the true value. We point out that the model sections should be plotted using gray shading for each cell to reflect the piece-wise constant nature of the model. However, when the model has only a small number of cells in each spatial direction, the structural trends are more readily shown when contours are used. For this reason, we have contoured the model sections.

Next, the same data are inverted using a model objective function that includes penalty terms on spatial roughness, ϕ_{mv}. The depth weighting is applied to all terms, as in equation (20). The inversion uses 54 subspace vectors and achieves the expected misfit in 13 iterations. The recovered model is shown in Figure 9. It is smoother, has a slightly lower amplitude than the model in Figure 8, and it recovers the essential features of the true model such as the depth and dip angle.

It is observed, in this example and in other synthetic and field test examples, that minimizing either the first term in the model objective function in equation (20), ϕ_{ms}, or using all four terms, generates models that are reasonable representations of the true structure. In the absence of prior information, both models can provide useful information about the subsurface susceptibility distribution. However, the model minimizing ϕ_{ms} can be obtained at less computational cost. Further-

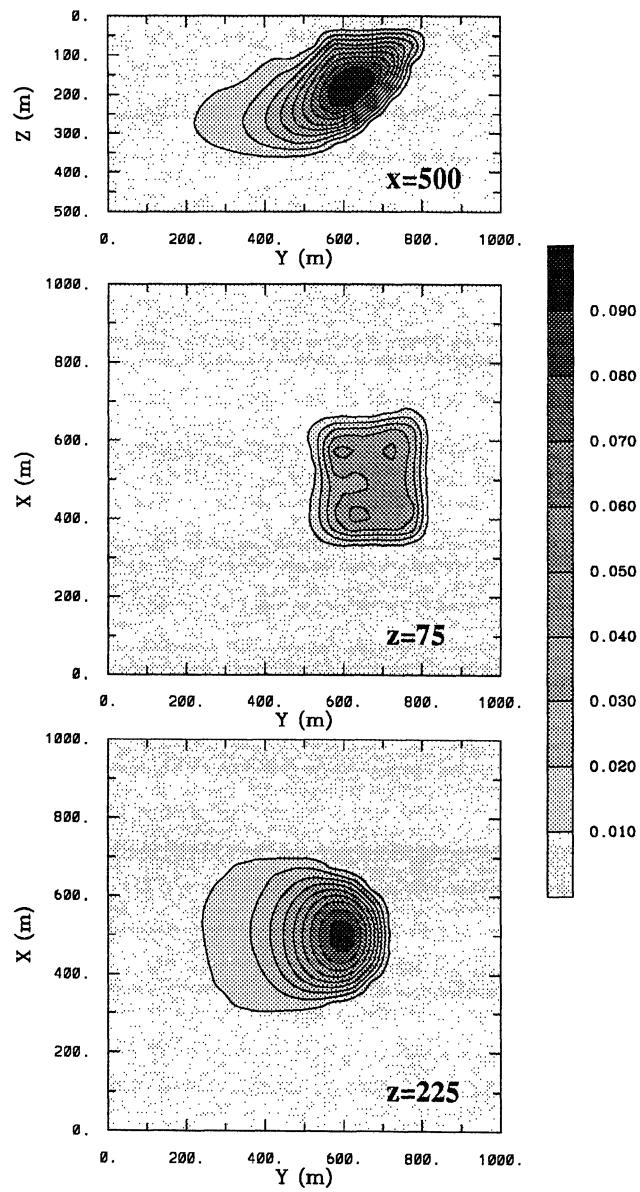

FIG. 8. Model obtained from inverting the data shown in Figure 2 by minimizing only ϕ_{ms}, which has the depth weighting applied. This is to be compared with the true model in Figure 1. The major features in the true model, such as dip angle and depth exte nt, are evident in the recovered model.

more, the depth weighting in this case is rather well supported by mathematical analysis whereas it is an argued extension for the three roughness components. Therefore, a reasonable approach to inverting field data might be a two-step process. The data can be inverted first by minimizing ϕ_{ms}, and the resultant model may be used in the interpretation as a preliminary result. If there are interesting features present and if one desires to refine the model by incorporating prior information to enhance or attenuate the structural complexity in different regions, a second inversion can be carried out using an objective function consisting of both ϕ_{ms} and ϕ_{mv}. The model obtained by minimizing ϕ_{ms} can then be used in this inversion as an initial model. The available prior information can be incorporated into the second inversion by forming a reference model and 3-D weighting functions, w_s, w_x, w_y, w_z.

We now invert the same data by using $m = \ln(\kappa)$ as the model. It is not possible to incorporate a zero susceptibility as the reference model, so we minimize an objective function consisting of ϕ_{mv} with the reference model removed. The same depth weighting is applied to all terms of ϕ_{mv}. Since $\kappa = e^m$, the positivity of the susceptibility is ensured without invoking the transformation of variables. The result is shown in Figure 10a. This is a cross-section at x = 500 m and plotted on a logarithmic scale in accordance with the model used in the inversion. The inverted susceptibility shows the presence of the dipping anomaly as a broad region of high susceptibility. However, the interpretation based upon such a model can be complicated by the variations of susceptibility that are small and have little effect on the surface data. We have replotted the cross-section on a linear scale in Figure 10b and the anomalous region is now delineated more clearly. Its top portion indicates the tabular body and defines the depth to the

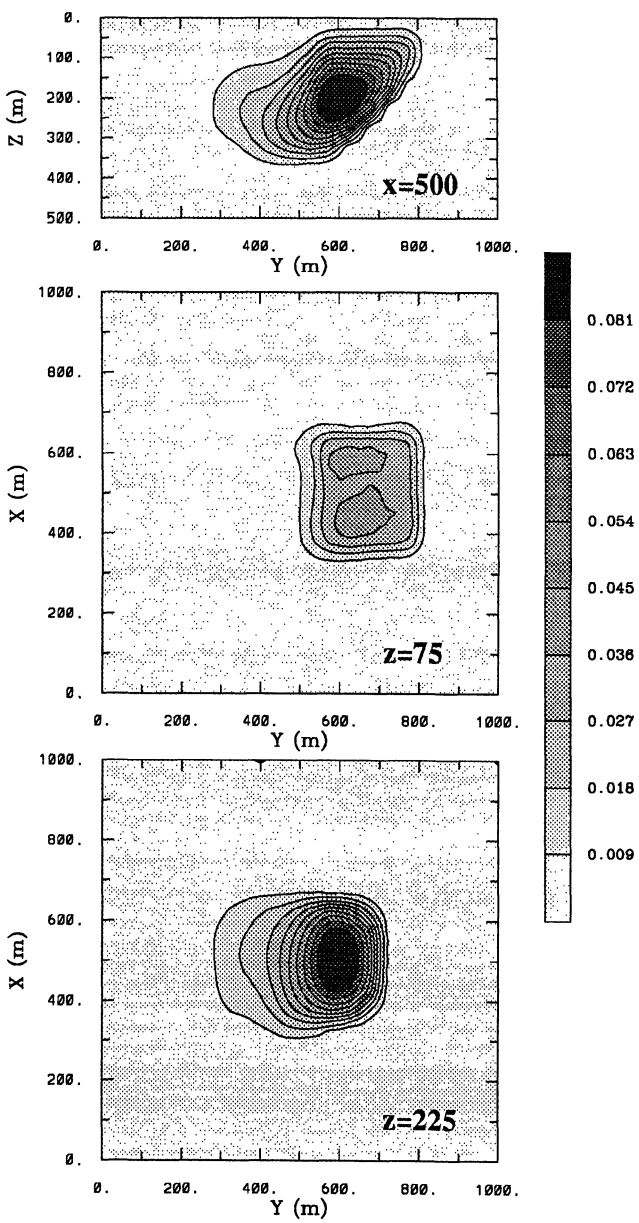

FIG. 9. The model derived from inverting the slab model data in Figure 2 by minimizing the model objective function having both ϕ_{ms} and ϕ_{mv}. The same depth weighting is used. This model appears to be smoother and has a smaller amplitude than that in Figure 8.

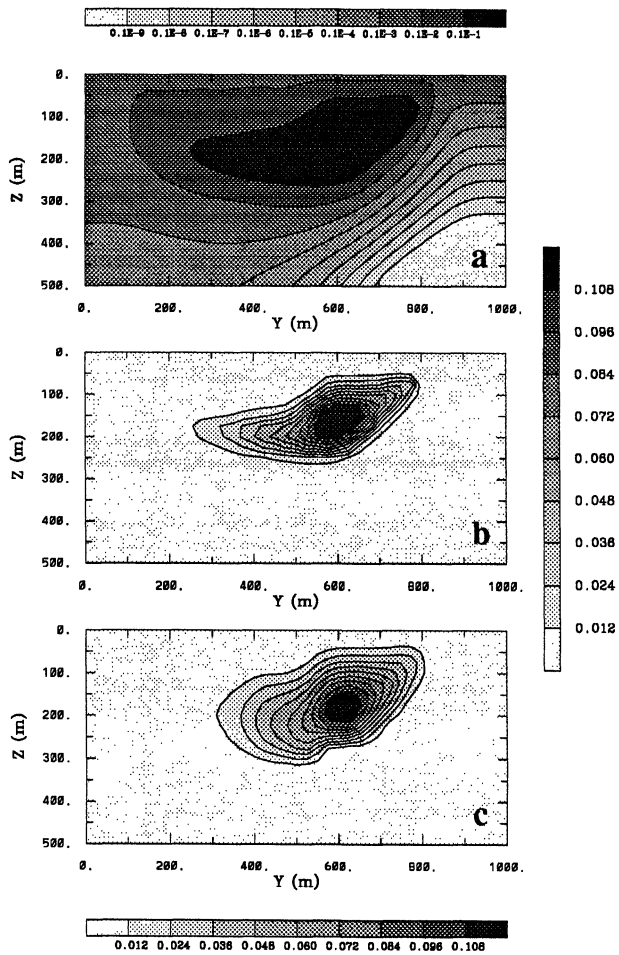

FIG. 10. The model obtained from inverting the data shown in Figure 2 by using $m = \ln(\kappa)$ as the model and minimizing ϕ_{mv} with the reference model removed. The inverted logarithmic susceptibility in cross-section at x = 500 m is shown in (a) and it is replotted on a linear scale in (b). As a comparison, the result obtained by using $m = \kappa$, and the same objective function is shown in (c).

top and dipping angle. The anomaly terminates at a shallower depth than the true model and has a nearly horizontal extension to the left. As an exact comparison, Figure 10c is the susceptibility model obtained by minimizing ϕ_{mv} but using $m = \kappa$ as model and invoking the positivity. This is a smoother model and exhibits more gradual changes in the susceptibility. It has a slightly deeper extent than the model in Figure 10b. With the exception of details toward the bottom, however, both models provide almost the same information about the anomalous susceptibility region. It might be concluded that inversion using either linear or logarithmic susceptibility is viable for practical applications. However, we note that the presentation in Figure 10b is inconsistent with the model used in the inversion. Since the inverted susceptibility is easier to interpret on a linear scale as demonstrated here, and since the magnetic data are linearly related to the susceptibility, we generally prefer to work with the susceptibility κ as the model in the inversion.

As the second example we invert the total field anomaly data produced by a slightly more complicated model and with two different inducing field directions. The true model is shown in Figure 11 in the same format as before. It is a dipping slab having its top and bottom portions offset to simulate the result of a normal faulting. The faulted slab strikes north. The data from this model, when the inducing field has a direction of I = 45° and D = 45°, are shown in Figure 12. Again Gaussian noise has been added to the data. The inversion minimizes an objective function consisting of ϕ_{ms} and ϕ_{mv} that have the same depth weighting and nonlinear mapping as used to produce the results in Figure 9. Figure 13 displays the recovered model in three slices. It shows two distinct anomalous regions of susceptibility that correspond to those in the true model. The dipping structure is evident from the top block. On plan view, the strike direction and the strike length of the anomaly are also well recovered.

When the inducing field direction is I = 0° and D = 45°, the surface anomaly with added Gaussian noise is that shown in Figure 14. Carrying out the inversion using an identical model objective function generates the model shown in Figure 15. It is similar to the model shown in Figure 13, which is recovered under an inducing field at 45° inclination. Again, the two separate blocks, the dipping direction, and the length and direction of the strike, are all reasonably recovered. This is a positive result in that, although the surface anomalies have very different expressions under different inducing field directions, the inversion algorithm is able to consistently recover the source structure. Moreover, the algorithm had no difficulty in inverting data generated from an inducing field having zero inclination; such data often pose problems in interpretations that include a reduction to pole.

We emphasize that positivity has played a pivotal role in all the inversions. Magnetic data generally have regions of nega-

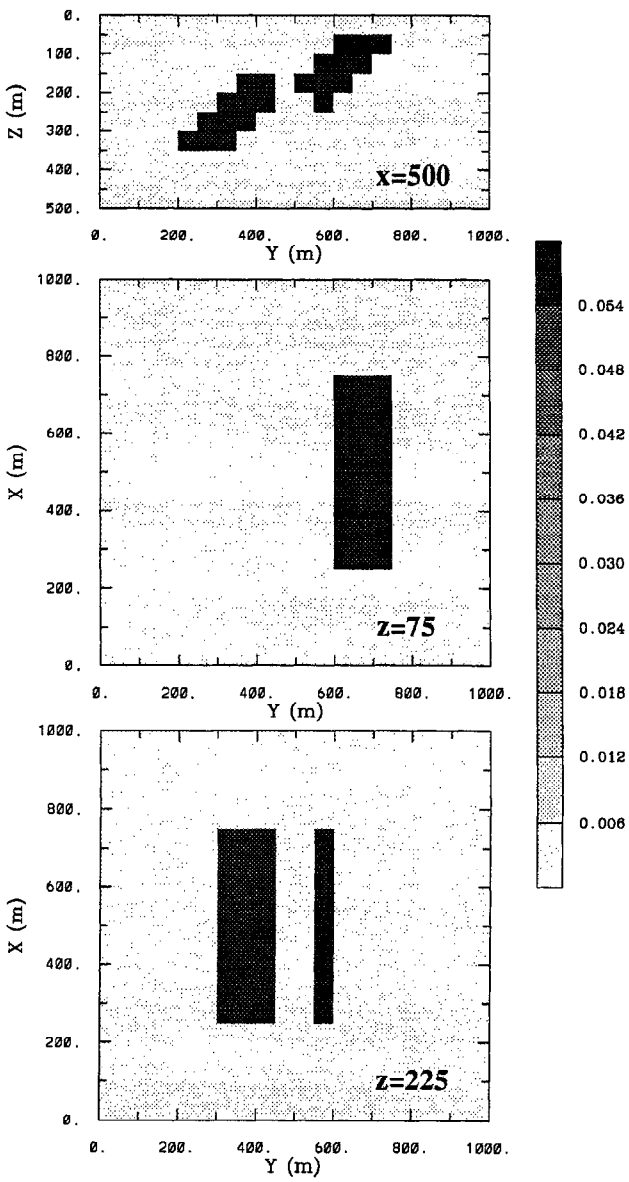

FIG. 11. The second synthetic test example. The top and bottom portions of the anomalous susceptibility are offset to simulate a norm fault structure. It also has a large strike length in the north direction.

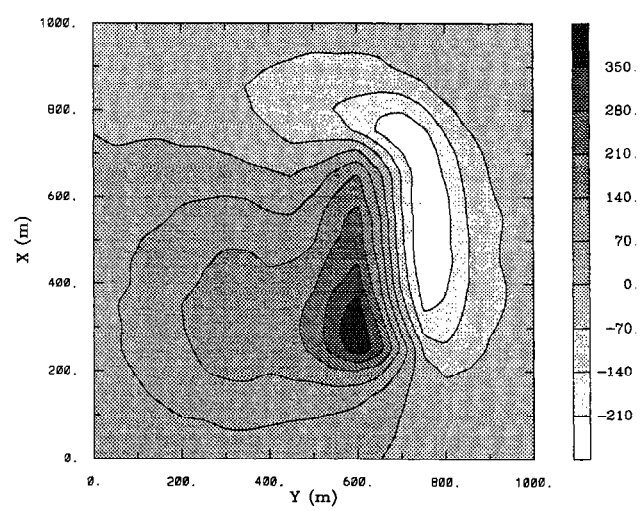

FIG. 12. The surface total field anomaly produced by the faulted slab in Figure 11, under an inducing field at I = 45° and D = 45°. Uncorrelated Gaussian noise is again added to the data.

tive values that result from dipping bodies or inclined inducing field, or both. Without positivity, the constructed susceptibility is often negative and the dipping bodies appear more vertical. Recovery of correct dip and, to some extent, depth to the top of the anomalous body, are often the result of invoking positivity. Once the positivity is imposed, it is no longer true that an equivalent stratum that reproduces the data exists at any depth. Therefore, cells of anomalous susceptibility cannot be placed arbitrarily close to the surface, and no equivalent source can be constructed with negative susceptibilities. This restricts the class of admissible models and, consequently, reduces the nonuniqueness.

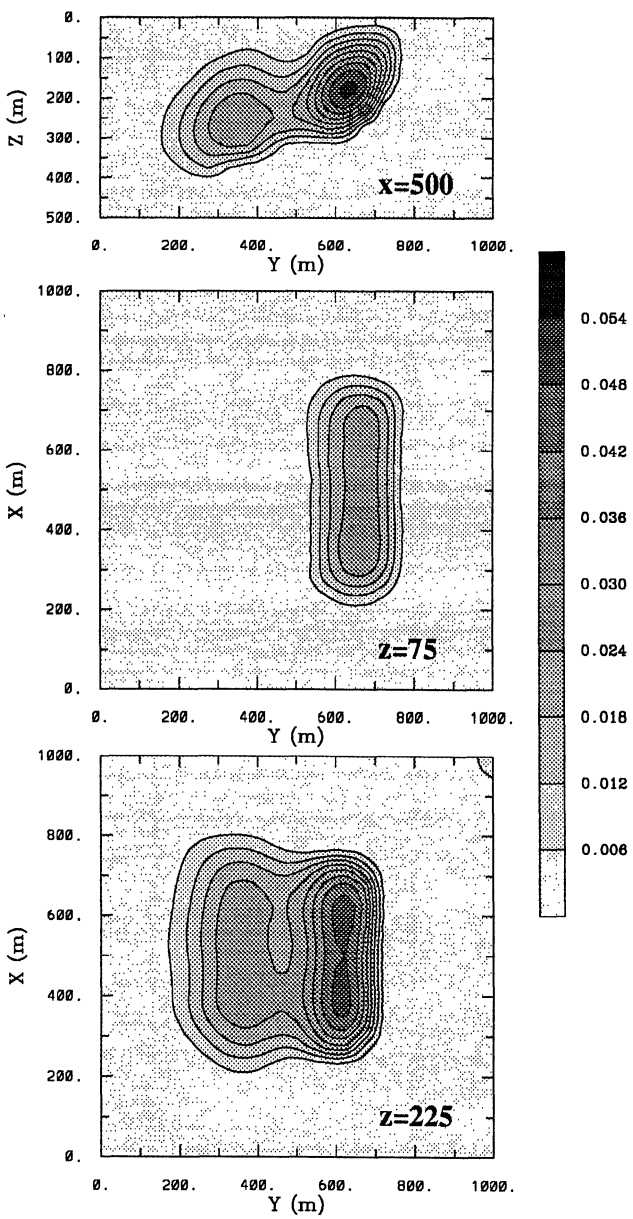

FIG. 13. The susceptibility model recovered from the data shown in Figure 12. It is seen that both the top and bottom block of the true model are recovered and the strike direction and length are well defined.

FIELD EXAMPLE

As the final example, we invert field data taken over a copper-gold porphyry deposit at Mt. Milligan in central British Columbia. The host rocks for the deposit are early Mesozoic volcanic and sedimentary rocks and contain intrusive monzonitic rocks that have accessory magnetite. Porphyry-style alteration and copper-gold mineralization are contemporaneous with the intrusive events. The copper and gold are known to be concentrated in the potassic alteration assemblage, which is mainly around the contact of the monzonite intrusions and may extend outward and into fractured volcanic rocks. Among other minerals, magnetite is one of the strong indicators of the potassic alteration. Ground magnetic data are acquired in the region at 12.5-m spacing along lines in the east direction and spaced 50 m apart. Our study of the data set has focused on a 1.2 km x 1 km area, which covers a large monzonite body known as the MBX stock and contains a reasonably isolated set of magnetic anomalies. Fairly detailed information about the geology is available through a major drilling program, but no susceptibility logs were available.

Magnetic data from a larger area were first upward continued to 20 m. A regional field was then defined and removed from the upward continued data. The continuation operation suppresses the noise in the data and also facilitates the discretization of the topographic surface for the model so that all observation points remain above the discretized surface. Although the original data were collected at 12.5-m spacing, we use the data at 25-m spacing. This yields 1029 data points at varying elevations. Figure 16 shows the data contoured according to their horizontal locations. The direction of the inducing field is $I = 75°$ and $D = 25.73°$. Several major magnetic highs are observed in the map. However, the influence of anomalies adjacent to the map is also visible along the edges. We choose a model domain that is horizontally larger than the data area, coincides at the top with the highest point on the topographic surface, and extends to 450-m depth. The model is discretized horizontally at a 25-m interval beneath the area of data. In the

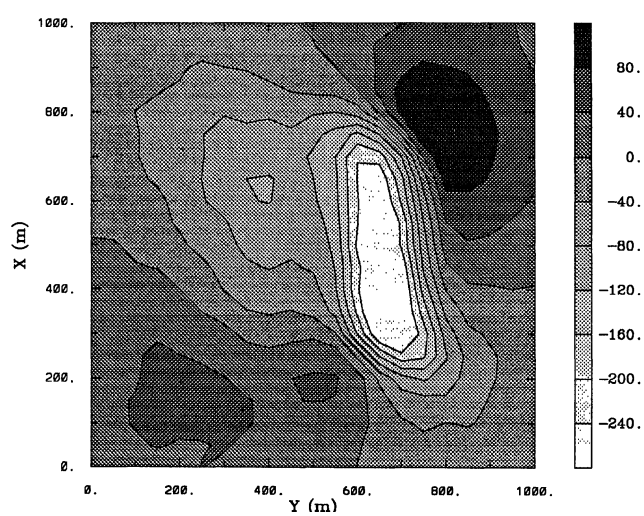

FIG. 14. The surface total field anomaly produced by the faulted slab in Figure 11 under an inducing field at $I = 0°$ and $D = 45°$. Uncorrelated Gaussian noise is added to the data.

vertical direction, the first 100 m is divided at a 12.5-m interval so that the surface can be adequately discretized onto the model mesh. Below the depth of 100 m, an interval of 25 m is used. This results in a mesh with 52 x 44 x 22 cells. Once the mesh is defined, the topography is discretized onto it. The 43 428 cells below this surface define the susceptibility model, and the inverse problem is therefore formalized by inverting 1029 data to recover the susceptibilities in those cells. The depth weighting is referenced to the top of the model domain. Each datum is assumed to have an error whose standard deviation is equal to 5% of its magnitude plus 10 nT. The error estimate includes not only the repeatability of the instrument reading but also the geological noise and errors introduced by the inaccurate recording position and by separating the anomalous field from the initial total field measurements. One hundred subspace vectors generated by dividing the data map into small subareas are used in the inversion. We use a nonlinear mapping with $\kappa_b = 0.0002$ and $\kappa_1 = 0.02$. The recovered model is shown in Figure 17 as one plan-section and three cross-sections. From the plan-section, two concentrated susceptibility highs are observed in the central region. Surrounding them are three linear anomalies trending northeast. In the cross-sections, the major anomalies are seen at moderate depths but there is considerable variation in the depth to the top. There are also smaller anomalies extending to the surface. In general, there are more detailed structures near the surface and the model becomes increasingly smooth at greater depths. As required by the objective function, there is no excessive structure associated with each unit of high susceptibility region. Comparison with drill logs indicates that the recovered magnetic susceptibility highs are mostly associated with the monzonite intrusions and with faults or fracture zones. Figure 18 compares the recovered susceptibility model with the geology (Cam DeLong, personal communication) in the cross-section at x = 600 m. The large susceptibility high is spatially well-correlated with the MBX stock and reflects the initial magnetite content in the intrusion. Two smaller susceptibility highs are present east of the stock. The high at y = 650 m coincides with the boundary of stock and porous trachytic units while the high at y = 900 m coincides with the upper portion of the Rainbow dyke. These are locations of the most intensive potassic alterations and the susceptibility highs are indicative. of the magnetite produced by the alteration process. Over all, this is a rather encouraging result.

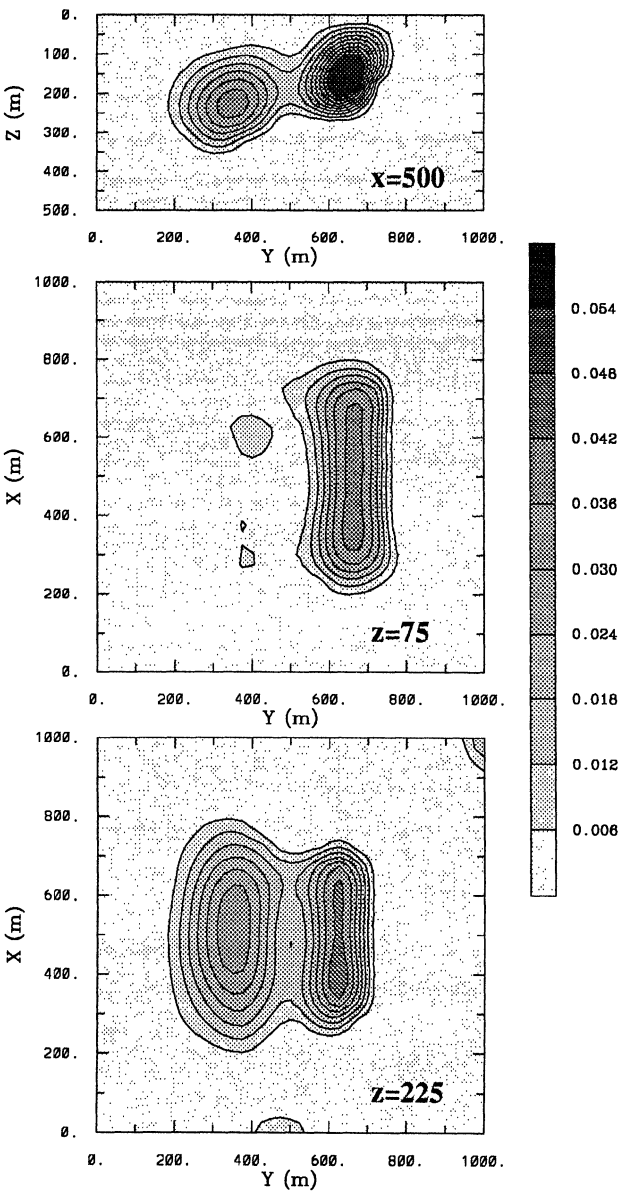

FIG. 15. The susceptibility model recovered from the data shown in Figure 14. This model is similar to that shown in Figure 13.

CONCLUSION

We have developed an algorithm to invert surface magnetic data for general 3-D susceptibility distributions. Although we have illustrated the algorithm using examples on the scale pertinent to mining applications, the method is general and applicable to problems on different scales ranging from environmental to regional investigations. To overcome the inherent nonuniqueness, we obtain the solution by minimizing a

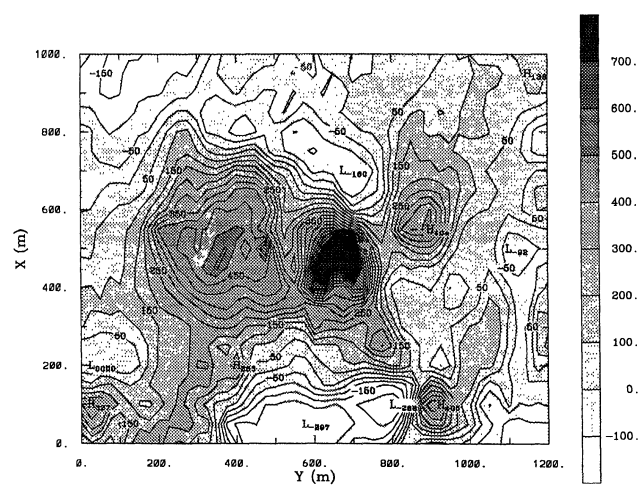

FIG. 16. The extracted total field anomaly from ground magnetic data at Mt. Milligan Copper-gold porphyry deposit. The data are contoured according to their horizontal locations in this map, although thev are at different elevations.

specific objective function of the model. Our model objective function has the ability to incorporate prior information into the inversion via a reference model and 3-D weighting functions. A crucial feature of the objective function is a depth weighting function that counteracts the natural decay of the kernel functions. The parameters of the depth weighting depend upon the discretization of the model but are easily calculated. The minimization is carried out using a subspace technique that reduces the computational effort and allows the positivity constraint of susceptibility to be incorporated. Both susceptibility and logarithmic susceptibility can potentially be used as the model in the inversion. Since the data are linearly related to susceptibility, and since usually absolute values of susceptibility are required for interpretation rather than relative values, especially in regions of very low susceptibility, we have generally chosen to work with susceptibility. To suppress the noise from small magnetic bodies near the surface, we recommend in general that the data be upward continued to a height comparable with the width of the surface cell before inversion.

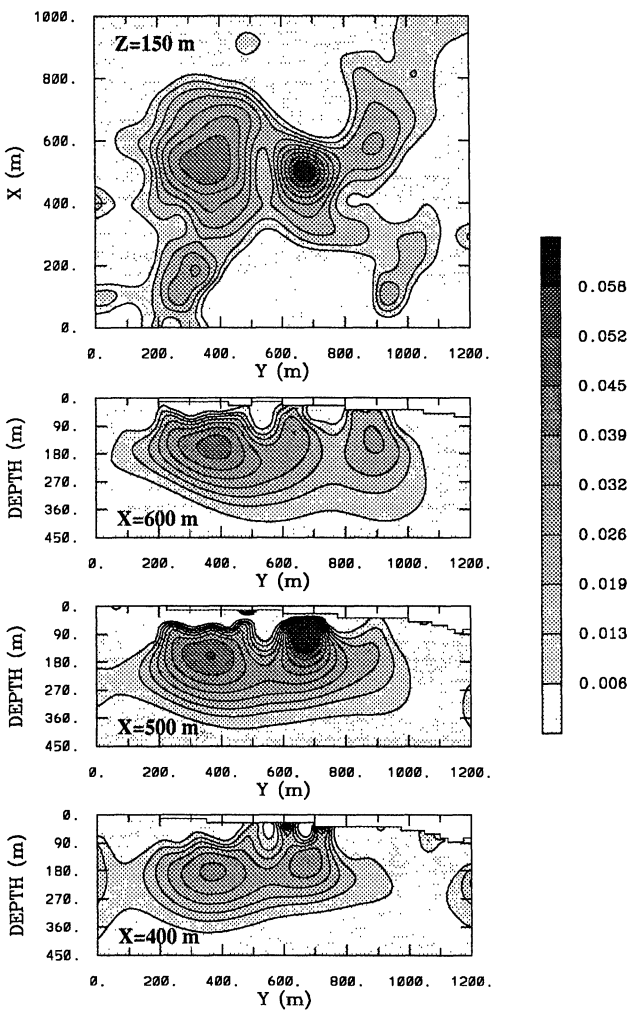

FIG. 17. The recovered susceptibility model shown in one plan-section and three cross-sections. The plan-section is at the depth of 150 m and the three cross-sections are at x = 600,500, and 400 m, respectively.

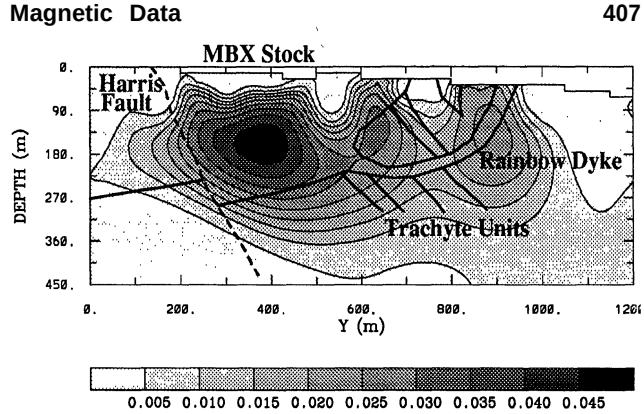

FIG. 18. Comparison of the recovered susceptibility model in a cross-section (x = 600) with the geology for the Mt. Milligan deposit. The susceptibility high within the MBX stock reflects the initial magnetite in the intrusive while the susceptibility highs near the Rainbow dyke are related to the magnetite produced by potassic alteration.

Applications of our inversion to synthetic data sets have produced models representative of the true structures and demonstrated the ability of the algorithm to construct consistent models at different magnetic latitudes. Inversion of field data has produced a susceptibility model that is consistent with the known geology and mineralization information. These results represent an encouraging conclusion: although the inversion of magnetic data seems impossibly nonunique when one has a large number of cells, inversions using a properly designed model objective function can produce susceptibility distributions that yield meaningful geologic information.

ACKNOWLEDGMENTS

This work was supported by an NSERC IOR grant and an industry consortium "Joint and Cooperative Inversion of Geophysical and Geological Data." Participating companies are Placer Dome, BHP Minerals, Noranda Exploration, Cominco Exploration, Falconbridge, INCO Exploration & Technical Services, Hudson Bay Exploration and Development, Kennecott Exploration Company, Newmont Gold Company, Western Mining Corporation, and CRA Exploration Pty.

REFERENCES

Bhattacharyya, B. K., 1964, Magnetic anomalies due to prism-shaped bodies with arbitrary magnetization: Geophysics, **29,** 5 17-53 1.

——— 1980, A generalized multibody model for inversion of magnetic anomalies: Geophysics, **45,** 255-270.

Green, W. R., 1975, Inversion of gravity profiles by use of a Backus-Gilbert approach: Geophysics, **40,** 763-772.

Guillen, A., and Menichetti, V., 1984, Gravity and magnetic inversion with minimization of a specific functional: Geophysics, **49,** 1354-1360.

Last, B. J., and Kubik, K., 1983, Compact gravity inversion: Geophysics, **48,** 713-721.

Oldenburg, D. W., and Li, Y., 1994, Subspace linear inversion methods, Inverse Problems, **10,** 915-935.

Rao, D. B., and Babu, N. R., 1991, A rapid methods for three-dimensional modeling of magnetic anomalies: Geophysics, **56,** 1729-1737.

Wang, X., and Hansen, R. O., 1990, Inversion for magnetic anomalies of arbitrary three-dimensional bodies: Geophysics, **55,** 1321-1326.

Zeyen, H., and Pous, J., 1991, A new 3-D inversion algorithm for magnetic total field anomalies: Geophys. J. Int., **104,** 583-591.

APPENDIX

MODEL OBJECTIVE FUNCTION

Our inversion method uses a model objective function of the form

$$\phi_m(m) = \alpha_s \int_V w_s\{w(z)[m(\mathbf{r}) - m_0]\}^2\, dv + \alpha_x \int_V w_x \left\{\frac{\partial w(z)[m(\mathbf{r}) - m_0]}{\partial x}\right\}^2 dv + \alpha_y \int_V w_y \left\{\frac{\partial w(z)[m(\mathbf{r}) - m_0]}{\partial y}\right\}^2 dv + \alpha_z \int_V w_z \left\{\frac{\partial w(z)[m(\mathbf{r}) - m_0]}{\partial z}\right\}^2 dv. \quad \text{(A-1)}$$

The numerical evaluation of this functional is carried out by introducing the model mesh and evaluating all terms using a finite-difference approximation. The discretized model objective function has the form

$$\phi_m(\mathbf{m}) = (\mathbf{m} - \mathbf{m}_0)^T(\underset{\sim}{\mathbf{W}}_s^T\underset{\sim}{\mathbf{W}}_s + \underset{\sim}{\mathbf{W}}_x^T\underset{\sim}{\mathbf{W}}_x + \underset{\sim}{\mathbf{W}}_y^T\underset{\sim}{\mathbf{W}}_y + \underset{\sim}{\mathbf{W}}_z^T\underset{\sim}{\mathbf{W}}_z)(\mathbf{m} - \mathbf{m}_0) \equiv (\mathbf{m} - \mathbf{m}_0)^T\underset{\sim}{\mathbf{W}}_m^T\underset{\sim}{\mathbf{W}}_m(\mathbf{m} - \mathbf{m}_0) \quad \text{(A-2)}$$

Each component matrix can be written as the product of three individual matrices and one oefficient. That is,

$$\underset{\sim}{\mathbf{W}}_i = \alpha_i \underset{\sim}{\mathbf{S}}_i \underset{\sim}{\mathbf{D}}_i \underset{\sim}{\mathbf{Z}}, \qquad i = s, x, y, z, \quad \text{(A-3)}$$

where $\underset{\sim}{\mathbf{S}}_i$ are diagonal matrices representing the spatially dependent 3-D weighting functions, $\underset{\sim}{\mathbf{D}}_i$ are the finite-difference operators for each component, and $\underset{\sim}{\mathbf{Z}}$ is a diagonal matrix representing the discretized form of depth weighting function $w(z)$.

The elements of $\underset{\sim}{\mathbf{S}}_i$ are given by $\sqrt{w_i}$. They are defined over each cell for $\underset{\sim}{\mathbf{S}}_s$, and over each interface between adjacent cells in the respective directions for $\underset{\sim}{\mathbf{S}}_x$, $\underset{\sim}{\mathbf{S}}_y$, and $\underset{\sim}{\mathbf{S}}_z$. $\underset{\sim}{\mathbf{D}}_s$ has elements $\sqrt{\Delta x \Delta y \Delta z}$ on its diagonal, where Ax, Ay, and Δz are the cell width. The matrix $\underset{\sim}{\mathbf{D}}_x$ has two elements $\pm\sqrt{\Delta y \Delta z/\delta x}$ in each row, where δx is the distance between the centers of cells adjacent in the x - direction. Similarly, $\underset{\sim}{\mathbf{D}}_y$ and $\underset{\sim}{\mathbf{D}}_z$ have elements $\pm\sqrt{\Delta x \Delta z/\delta y}$ and $\pm\sqrt{\Delta x \Delta y/\delta z}$, respectively, where δy and δz are the distances between centers of adjacent cells in the y- and z - directions. Once the mesh is defined and all weighting functions, w_s, w_x, w_y , w_z, and w (z) are chosen, equation (A-3) is evaluated straightforwardly and $\underset{\sim}{\mathbf{W}}_m^T\underset{\sim}{\mathbf{W}}_m$ is formed.

New enhancement filters for geological mapping

Zhiqun Shi*
Encom Technology Australia
zhiqun.shi@encom.com.au

Graham Butt
Encom Technology Australia
graham.butt@encom.com.au

SUMMARY

Two types of filters have been developed for the purpose of enhancing weak magnetic anomalies from near-surface sources while simultaneously enhancing low-amplitude, long-wavelength magnetic anomalies from deep-seated or regional sources. The Edge filter group highlights edges surrounding both shallow and deeper magnetic sources. The results are used to infer the location of the boundaries of magnetised lithologies. The Block filter group has the effect of transforming the data into "zones" which, similar to image classification systems, segregate anomalous zones into apparent lithological categories. Both filter groups change the textural character of a dataset and thereby facilitate interpretation of geological structures.

The effect of each filter is demonstrated using theoretical model studies. The models include both shallow and deep sources with a range of magnetisations. Comparative studies are made with traditional filters using the same theoretical models. In order to simulate real conditions, Gaussian noise has been added to the model response. Techniques for noise reduction and geological signature enhancement are discussed in the paper.

The new approaches are applied to actual magnetic survey data covering part of the Goulburn 1:100 000 scale map sheet area, New South Wales. Some new geological inferences revealed by this process are discussed

Key words: Enhancement filters, magnetic sources, geological mapping.

INTRODUCTION

High-resolution aeromagnetic survey data represent a rich source of detailed information for mapping surface geology as well as for mapping deep tectonic structure. Traditional enhancement techniques, such as first vertical and horizontal derivatives (1VD, 1HD), analytic signal (AS), and high-pass in-line or grid filters are used in enhancing magnetic anomalies from near-surface geology.

In recent years the potential field tilt filter has been introduced (Miller and Singh, 1994) and it has achieved recognition for its value in the analysis of potential field data for structural mapping and enhancement of both weak and strong magnetic anomalies (Verduzco *et al*, 2004). The total horizontal derivative of the TMI reduced to the pole is also widely used for detecting edges or boundaries of magnetic sources (Cordell and Grauch, 1985; Blakely and Simpson, 1986; Phillips, 1998).

Several disadvantages pertain to the use of these traditional filters. They often only diffusely identify source location and boundaries, particularly in colour image presentations. They usually emphasise short wavelength anomalies at the expense of signal from deeper magnetic sources and the range of amplitudes remaining in the filtered output may dominate the source boundary information being sought. In addition, some traditional filters emphasise noise with resultant impact on the interpretation of source boundaries.

This paper identifies new processes which have been developed to address these disadvantages and provide output which can improve map-based interpretations.

Unless otherwise stated, all filters have been operated on TMI data reduced to the pole (RTP).

METHOD AND RESULTS

Theoretical Model Testing

A theoretical 2D grid of total magnetic intensity (TMI) computed at the surface was created by forward 3D modelling of the TMI response from a set of theoretical magnetic sources having variable width, strike extent, depth, depth extent (DE), dip, magnetic susceptibility and strike azimuth. A list of these parameters is presented in Table 1. In two of the sources, remanence was simulated using negative magnetic susceptibility. The TMI of the theoretical models was computed at a geomagnetic inclination of -60 degrees using a notional east–west line spacing of 200 m and a grid cell size of 40 m. The TMI grid was then reduced to the pole (RTP) (Figure 1).

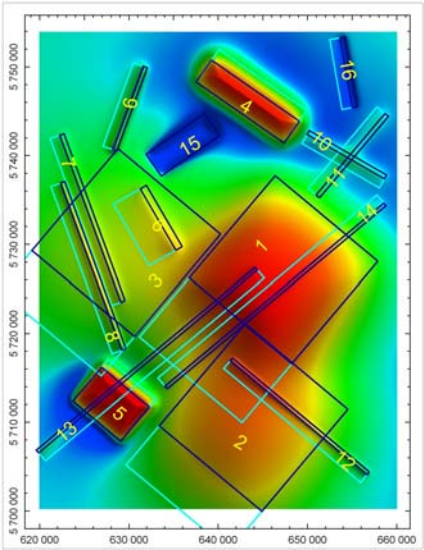

Figure 1. RTP image derived from multiple theoretical 3D magnetic sources, shown as wire frame outlines

A set of traditional filters was operated on the theoretical RTP grid. They include AS, 1VD, modulus of horizontal derivatives (MS) and Tilt and the results are presented in

Figure 2. The output grids variously show discontinuous trending (crossed sources in upper right of AS image), diffuse, weak edges (deep source in centre right of the MS image) and lack of precise source edge definition (1VD and Tilt).

Model Label	Depth (m)	Width (m)	DE (m)	Dip (deg)	Magnetic Susceptibility (SI)	Strike Length (m)	Azimuth (deg)
1	4000	15000	15000	120	0.010	15000	-050
2	6000	15000	10000	120	0.010	15000	-050
3	10000	15000	10000	120	0.010	15000	-050
4	1000	3000	4000	70	0.010	12000	-055
5	500	5000	2000	60	0.010	7000	-050
6	1000	800	2000	150	0.005	8000	-030
7	600	500	2000	120	0.001	20000	-020
8	200	500	2000	120	0.001	20000	-020
9	500	500	2000	120	0.003	10000	020
10	1000	500	2000	120	0.003	10000	-060
11	1000	500	2000	120	0.003	12000	040
12	200	400	2000	120	0.001	20000	-050
13	500	400	1000	40	0.002	32000	050
14	500	400	1000	140	0.001	32000	050
15	600	3000	4000	90	-0.002	8000	055
16	400	600	2000	120	-0.010	8000	-010

Table 1. List of parameters of theoretical magnetic sources

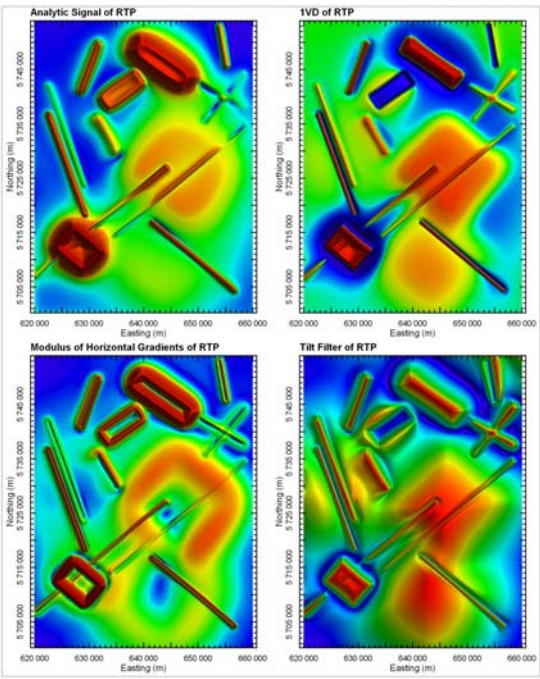

Figure 2. Comparison of enhancement filters of RTP: AS, 1VD, MS and Tilt filter. The models used are those depicted in Figure 1.

Edge Filters

The first avenue of development was to increase the sharpness of the anomalies used to map the edge of the magnetic sources. The MS grid yields anomaly peaks over the source edge locations, whereas these edges coincide with gradients in the 1VD, Tilt and AS filtered outputs. None of these filters produces easily interpreted edges in image form when the sources are weakly magnetised or are deep.

A new linear, derivative-based filter termed the ZS-Edgezone filter has been developed to improve edge detection in these situations. Its effect is shown in Figure 3 using the same theoretical models discussed earlier. The advantages of the filter are greatly increased anomaly sharpness over source edges and compression of the amplitude range so that differences in the original TMI amplitudes do not persist to dominate the edge interpretation. This has the ancillary effect that the method can be modified to provide automated edge conversion to vectors for use in GIS systems.

Although this filter significantly improves the precision of edge determination, it is subject to normal potential field limitations which determine that source edges cannot be resolved where the source is narrow relative to its depth. The filter also can produce a "halo" type artefact due to superposition of the response of a limited depth extent shallow source (Figure 1, Model 6) on that of deeper sources. A similar "halo" effect can be seen around the edges of remanently magnetised Model 15, also in Figure 1.

The ZS-Edge filter (Figure 4) has also been developed to map source edges. This filter differs from the ZS-Edgezone filter in that a greater contribution of the TMI anomaly amplitude over the source is retained, thereby improving anomaly characterisation at the expense of edge sharpness.

Both these filters produce edges which migrate down-dip towards the deepest edge of the source. This effect produces anomaly asymmetry that can assist interpretation of dip, although this effect is more pronounced for the ZS-Edge filter than for the ZS-Edgezone filter. Down-dip source extensions are depicted in cyan in Figure 1.

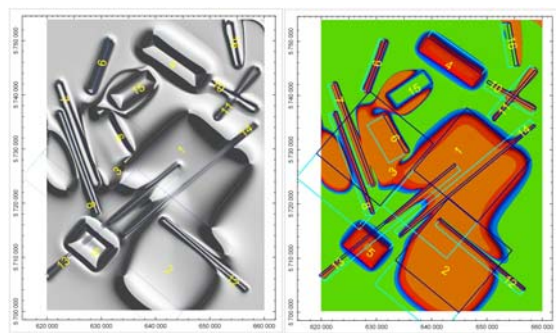

Figure 3. Anomaly edge and block enhancements using the ZS-Edgezone (left) and ZS-Block filters (right). Model positions are shown using wire frames.

Block Filters

In attempting to improve edge detection filters, an obvious progression is to highlight the magnetic regions whose edges have been mapped. To do this, a set of filters called "block" filters has been developed.

The Block filter group has the effect of transforming the potential field data into "zones" which, similar to image classification systems, segregate anomalous zones into apparent lithological categories. These filters can be imported for use in image classification systems or displayed in RGB space with other grids for empirical classification purposes.

The block filters, like the edge filters, are linear, derivative-based filters which use a combination of derivative and amplitude compression techniques to render the magnetic data into regions whose edges are sharply defined and whose amplitudes have a reduced range in comparison to the original TMI.

The ZS-Block filter (Figure 3) and the ZS-Plateau filter (Figure 4) depict the magnetic data as a 2D plan of apparent magnetic source distribution. Artefacts may occur as discussed for the edge filters.

The choice of ZS-Block, ZS-Plateau or ZS-Area filters will depend on the data characteristics of each magnetic survey and on the end-use requirement. The ZS-Plateau filter, for example, yields less variation in amplitude "texture" over a magnetic unit that either the ZS-Block or ZS-Area filters.

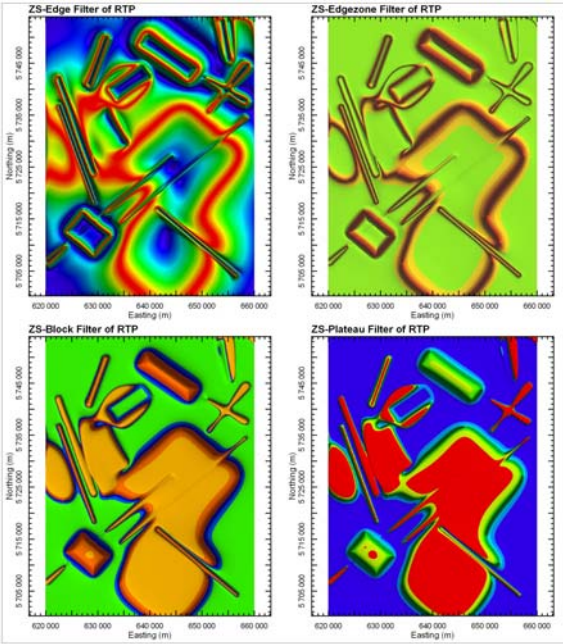

Figure 4. Comparison of ZS-Edge, ZS-Edgezone, ZS-Block and ZS-Plateau filtered outputs of RTP data

Effects of Noise

The influence of noise on the operation of these enhanced grids was tested by adding a large component of noise to the theoretical TMI profile data. This noise had a Gaussian distribution with a standard deviation equal to ten percent of the TMI standard deviation. The noise-modified TMI profile data were then de-spiked using a non-linear technique. Both the noise-affected and the de-spiked TMI data were then gridded and converted to RTP. The RTP data were then processed both with the traditional and newly developed filters.

Figure 5 shows the effect of the noise on the computations. The image of the noise-affected 1VD RTP data (top right) shows that weak and deep sources have been severely masked by the noise. Significant improvement can be achieved by using de-spiked data (lower left) or by low-pass grid filtering — for example, using an upward continuation filter (lower right).

Figure 6 shows that if real data with significant noise is encountered, a standard de-spiking or low-pass smoothing procedure may be used to achieve successful application of both the traditional and newly developed filters.

Figure 6 also depicts the use of enhanced outputs in RGB space to provide examples of how the combination of amplitude information (red colour) with edge information (green and blue colours) can be used to highlight source boundaries and remanence in a single image.

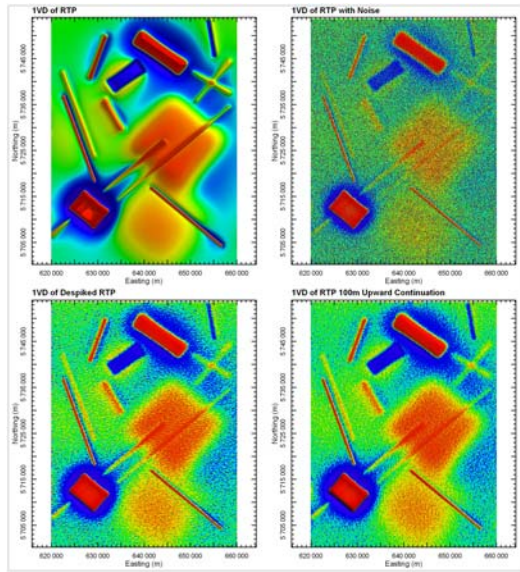

Figure 5. Comparison of 1VD of original model RTP data (top left) with noise-affected RTP data (top right) and noise-reduced RTP data (lower images)

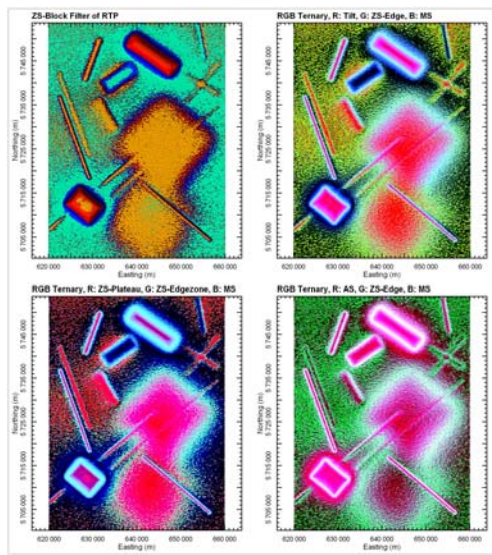

Figure 6. ZS-Block filter using noise-reduced RTP data (top left) and examples of filter combinations in RGB space using noise-reduced RTP data

Application to Field Data, Goulburn 1:100 000 Scale Map Sheet Area, New South Wales

Both the traditional and new enhancement filters were applied to test their suitability for geological definition to airborne magnetic survey data over the Goulburn 1:100 000 scale map sheet area (Johnson *et al,* 2003). These data were acquired as part of a joint program between the NSW Department of Mineral Resources and Geoscience Australia, with 250 m–spaced east–west flightlines. The magnetometer sensor occupied a nominal terrain clearance of 80 m. This dataset was selected since new detailed geological mapping had been recently completed. All the enhancements have been computed using TMI data reduced to the pole.

Figure 7 shows a comparison of part of the Goulburn 1:100 000 map sheet area surface geology with the ZS-Area

filter output. In the area surrounding location C, the ZS-Area filter transforms the magnetic data into separate magnetic units, which comprise the Devonian Bindook Volcanic Complex. The magnetic regions correlate closely with mapped andesites (Dkqa–cream coloured unit in Figure 7) whilst the intervening less-magnetic units correlate with rhyolitic ignimbrites (Dkqy–red unit in Figure 7)

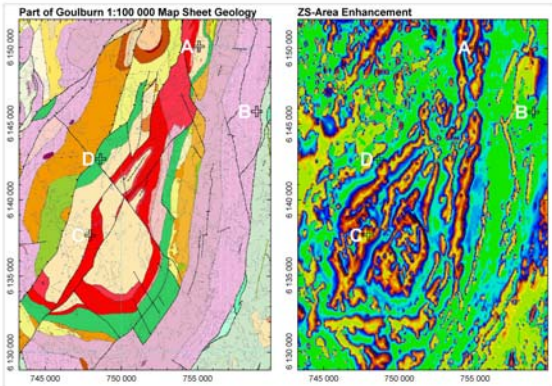

Figure 7. Comparison of geology and ZS-Area enhancement over the Bindook Volcanic Complex

Figure 8 displays some of the advantages of the edge detection filters. At location A, ambiguity concerning the continuity of Quialigo Formation units (cream and red units in Figure 7) is resolved by the ZS-Edgezone filter. At location B, a subtle lineament is confirmed, whilst at location D, the extent of the Bullamalita Conglomerate (green unit in Figure 7) is clearly mapped by the ZS-Edge filter. Structural breaks are often more easily interpreted using these transforms, for example, immediately southwest of location D.

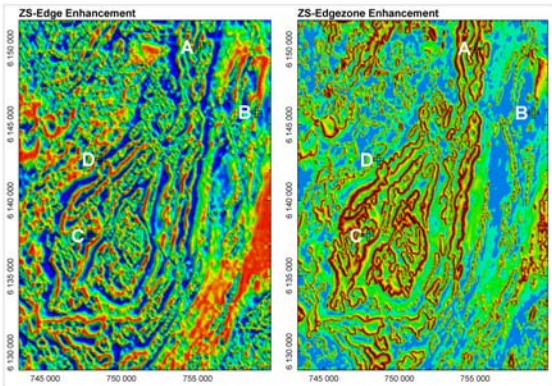

Figure 8. Comparison of ZS-Edge and ZS-Edgezone enhancements over the Bindook Volcanic Complex

Figure 9 shows standard RTP and Tilt transforms over the same area for reference.

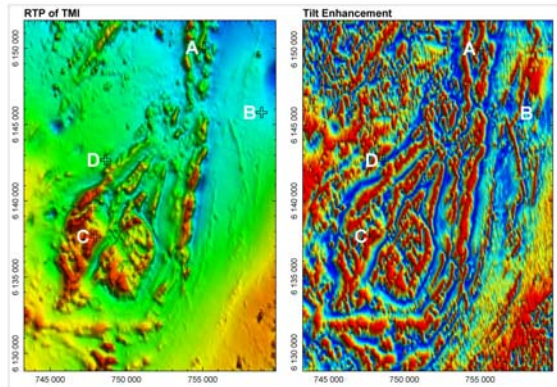

Figure 9. Comparison of RTP and Tilt filters over the Bindook Volcanic Complex

CONCLUSIONS

Traditional filters used to enhance magnetic data, including the more recently developed potential field tilt filter, are currently used to assist in determination of the location and extent of magnetic units.

Newly developed derivative-based filters may be used to improve the precision of source edge detection and, by extension, the determination of the spatial extent of magnetic units. These filters are demonstrated to perform successfully on both strongly magnetised features as well as on weakly magnetised or deep magnetic features. Artefacts may result particularly where anomaly superposition occurs.

The impact of noise in real data may be accommodated by these new methods provided noise-reduction techniques are employed.

The new filter outputs may be used as part of regional or detailed geological mapping projects, including in classification systems or in RGB space, to improve lithological discrimination and mapping.

The speed of magnetic unit mapping can be considerably increased through reliance on edge detection filters. Further improvements in mapping speed can be envisaged through automated conversion of edge anomalies to vector files.

ACKNOWLEDGMENTS

The authors would like to acknowledge the New South Wales Department of Mineral Resources for permission to use aeromagnetic and geological data from the Goulburn 1:100 000 map sheet area and helpful comments by David Robson during the project.

The authors wish to acknowledge Encom Technology for permission to publish the results of research into the proprietary filters used in this paper. The 3D modelling was carried out using Encom ModelVision Pro software, whilst processing and data visualisation were accomplished using Geosoft OASIS montaj and Encom Geoscape.

REFERENCES

Blakely, R. J. and Simpson, R. W., 1986, Locating edges of source bodies from magnetic or gravity anomalies, Geophysics, 51, 1494-1498.

Buckingham, A.J, Dentith, M.C., and List, R.D, 2003, Towards a system for content-based magnetic image retrieval: Exploration Geophysics, 34, 195-206.

Cordell, Lindrith, and Grauch, V.J.S., 1985, Mapping basement magnetization zones from aeromagnetic data in the San Juan Basin, New Mexico pp.181-197. In Hinze, W.J., ed,. The utility of regional gravity and magnetic maps: Society of Exploration Geophysicists,

Johnson A.J. *et al.*, 2003, Goulburn 1:100 000 Sheet 8828 Geology Map, New South Wales Department of Mineral Resources.

Miller, H.G., and Singh V., 1994, Potential field tilt — a new concept for location of potential field sources: Journal of Applied Geophysics, 32, 213-217.

Phillips, J.D., 1998, Processing and interpretation of aeromagnetic data for the Santa Cruz Basin–Patagonia Mountains Area, South-Central Arizona: United States Geological Survey Open-File Report 02-98.

Verduzco, B., Fairhead, J. D., Green, C. M., and MacKenzie, C., 2004, New insights into magnetic derivatives for structural mapping: The Leading Edge, 23 (2), 116-119.

Section 2: ZTEM Processing

Processing of Yukon ZTEM data

2D Inversion

Inversion Algorithm

The recorded ZTEM data were inverted using a 2D MT algorithm, developed by Constable and Wannamaker (deGroot-Hedlin and Constable, 1990; Wannamaker at al., 1987; deLugao and Wannamaker, 1996). The transverse electric (TE) response computed by the finite-element algorithm is used to model the along-line tipper data Tzx, taking into account that the vertical component is measured in the air and the horizontal component is recorded sitting on uniform ground. The responses of all provided frequencies (30 – 360 Hz) were included in the inversion.

Model specifications

The model mesh is shown in the following figure, with a close-up shown below. The topography is indicated by a solid black line.

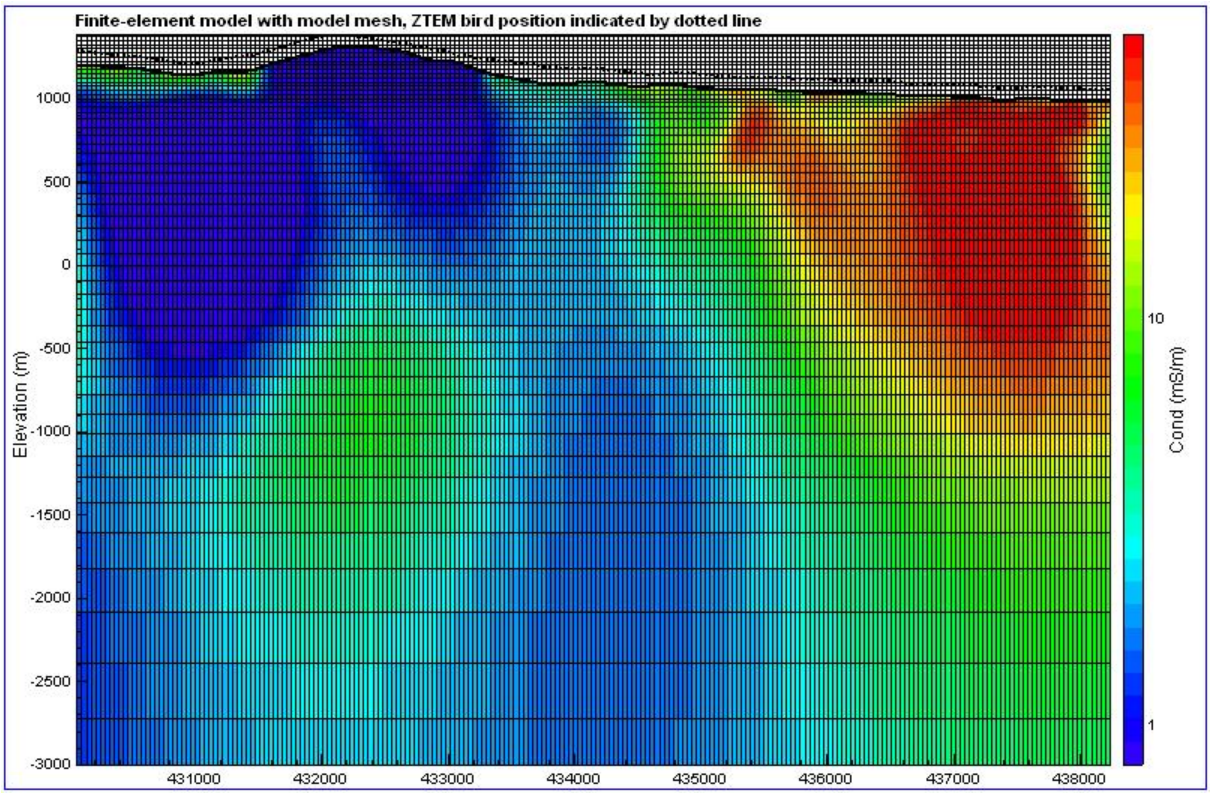

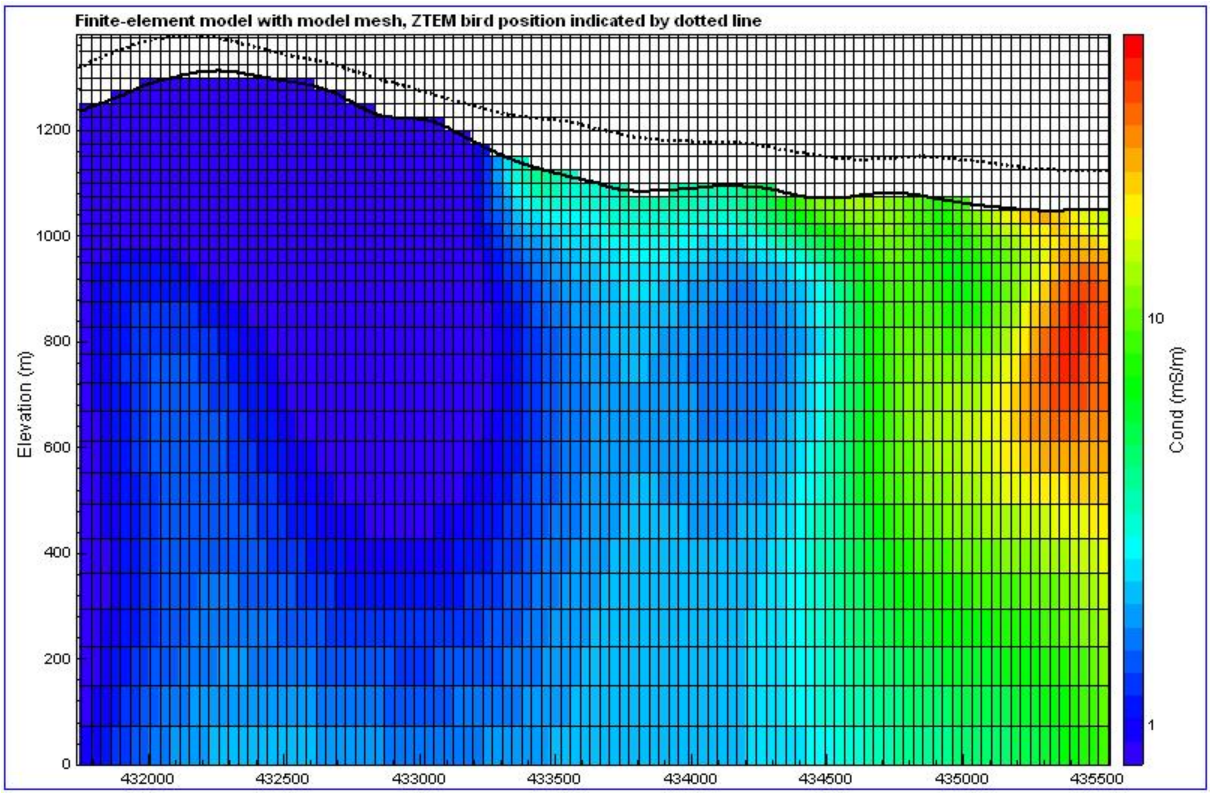

The model cells are 50 m wide in the horizontal direction. The number of vertical cells is a function of the flight line topography and bird elevation, hence, is different for each line. Since the algorithm takes into account the topography along each line, air cells are an integral part of the finite-element model. 25-m-thick cells are modelled between the topographic low and the highest bird elevation. Beneath the topographic low, cell thicknesses increase with increasing depth, as listed in the following table:

Layer	depth to bottom (m)	thickness (m)		Layer cont.	depth to bottom (m)	thickness (m)		Layer cont.	depth to bottom (m)	thickness (m)
1	25	25		15	776	71		29	2143	127
2	50	25		16	850	74		30	2276	133
3	83	33		17	927	77		31	2426	150
4	123	40		18	1007	80		32	2606	180
5	172	49		19	1090	83		33	2826	220
6	223	51		20	1177	87		34	3086	260
7	276	53		21	1267	90		35	3386	300
8	331	55		22	1361	94		36	3726	340
9	388	57		23	1459	98		37	4146	420
10	447	59		24	1561	102		38	4566	420
11	508	61		25	1668	107		39	5106	540
12	571	63		26	1779	111		40	5646	540
13	637	66		27	1895	116				
14	705	68		28	2016	121				

Padding was added in symmetric fashion to the left and right of each section. The padding cells to the right have the following widths (m): 60 60 80 200 200 200 400 400 400 800 800 800 2700 8100 24300

A 1000 Ohm-m halfspace was used as a start model, and a reference resistivity of 10,000 Ohm was used for depths beneath 4566 m.

The inversion results from all lines were merged into a survey GDB, containing modelled conductivities as a function of elevation, as listed in the following table.

Layer	Layer top Z1 (m ASL)	Layer bottom Z2 (m ASL)		Layer cont.	Layer top Z1 (m ASL)	Layer bottom Z2 (m ASL)		Layer cont.	Layer top Z1 (m ASL)	Layer bottom Z2 (m ASL)
1	2900	2875		48	1725	1700		95	550	525
2	2875	2850		49	1700	1675		96	525	500
3	2850	2825		50	1675	1650		97	500	475
4	2825	2800		51	1650	1625		98	475	450
5	2800	2775		52	1625	1600		99	450	425
6	2775	2750		53	1600	1575		100	425	400
7	2750	2725		54	1575	1550		101	400	375
8	2725	2700		55	1550	1525		102	375	350
9	2700	2675		56	1525	1500		103	350	325
10	2675	2650		57	1500	1475		104	325	292
11	2650	2625		58	1475	1450		105	292	252
12	2625	2600		59	1450	1425		106	252	203
13	2600	2575		60	1425	1400		107	203	152
14	2575	2550		61	1400	1375		108	152	99
15	2550	2525		62	1375	1350		109	99	44
16	2525	2500		63	1350	1325		110	44	-13
17	2500	2475		64	1325	1300		111	-13	-72
18	2475	2450		65	1300	1275		112	-72	-133
19	2450	2425		66	1275	1250		113	-133	-196
20	2425	2400		67	1250	1225		114	-196	-262
21	2400	2375		68	1225	1200		115	-262	-330
22	2375	2350		69	1200	1175		116	-330	-401
23	2350	2325		70	1175	1150		117	-401	-475
24	2325	2300		71	1150	1125		118	-475	-552
25	2300	2275		72	1125	1100		119	-552	-632
26	2275	2250		73	1100	1075		120	-632	-715
27	2250	2225		74	1075	1050		121	-715	-802
28	2225	2200		75	1050	1025		122	-802	-892
29	2200	2175		76	1025	1000		123	-892	-986
30	2175	2150		77	1000	975		124	-986	-1084
31	2150	2125		78	975	950		125	-1084	-1186
32	2125	2100		79	950	925		126	-1186	-1293
33	2100	2075		80	925	900		127	-1293	-1404
34	2075	2050		81	900	875		128	-1404	-1520
35	2050	2025		82	875	850		129	-1520	-1641
36	2025	2000		83	850	825		130	-1641	-1768
37	2000	1975		84	825	800		131	-1768	-1901
38	1975	1950		85	800	775		132	-1901	-2051
39	1950	1925		86	775	750		133	-2051	-2231
40	1925	1900		87	750	725		134	-2231	-2451
41	1900	1875		88	725	700		135	-2451	-2711
42	1875	1850		89	700	675		136	-2711	-3011
43	1850	1825		90	675	650		137	-3011	-3351
44	1825	1800		91	650	625		138	-3351	-4191

45	1800	1775		92	625	600		139	-4191	-5271
46	1775	1750		93	600	575				
47	1750	1725		94	575	550				

Noise and target fit

The noise level, specified for the inversion, was the maximum of 1.5% of the ZTEM response (relative noise level) and 0.15% (absolute noise level). The noise level for the high-frequency responses at 360 Hz were set twice those values. These noise estimates resulted in a stringent target data fit that was never met by the inversion, due to the actual noise level exceeding the noise estimates and the occasional inappropriateness of the 2D algorithm in a 3D conductivity scenario. To avoid overfitting the data, while optimizing data fit in a variable noise environment, the final result was chosen from inversion results a few iterations below the final iteration.

Apparent Conductivity and phase

The derivation of apparent conductivity and phase from VLF data is discussed by Becken and Pedersen (2003). The method has been applied to the ZTEM data, making joint use of the Tzx and Tzy tipper data.

D. Sattel
September 2013

References

Becken, M., and Pedersen, L.B., 2003, Transformation of VLF anomaly maps into apparent resistivity and phase: Geophysics 68, 497-505.

DeGroot-Hedlin, C. and Constable, S., 1990, Occam's inversion to generate smooth two-dimensional models from magnetotelluric data: Geophysics 55, 1613-1624.

De Lugao, P.P., and Wannamaker, P., 1996, Calculating the two-dimensional magnetotelluric Jacobian in finite elements using reciprocity, Geophys. J. Int., 127, 806-810.

Wannamaker, P.E., Stodt, J.A., and Rijo, L., 1987, A stable finite-element solution for two-dimensional magnetotelluric modeling: Geophysical Journal of the Royal Astronomical Society, 88, 277-296.

APPENDIX B – ZTEM PRIMER

APPENDIX C – DATA AND MAPS